The Star-formation Law in Galactic High-mass Star-forming Molecular Clouds

R. Retes-Romero, Y. D. Mayya, A. Luna, and L. Carrasco
Instituto Nacional de Astrofísica, Óptica y Electrónica, Luis Enrique Erro 1, Tonantzintla, Puebla, C.P. 72840, Mexico
rretes@inaoep.mx, ydm@inaoep.mx, aluna@inaoep.mx, carrasco@inaoep.mx

Abstract

We study the star-formation (SF) law in 12 Galactic molecular clouds with ongoing high-mass star-formation (HMSF) activity, as traced by the presence of a bright IRAS source and other HMSF tracers. We define the molecular cloud (MC) associated with each IRAS source using ^{13}CO line emission, and count the young stellar objects (YSOs) within these clouds using GLIMPSE and MIPSGAL 24 μm *Spitzer* databases. The masses for high-luminosity YSOs ($L_{bol} > 10\,L_\odot$) are determined individually using pre-main-sequence evolutionary tracks and the evolutionary stages of the sources, whereas a mean mass of 0.5 $M_\odot$ was adopted to determine the masses in the low-luminosity YSO population. The star-formation rate surface density (Σ_{SFR}) corresponding to a gas surface density (Σ_{gas}) in each MC is obtained by counting the number of the YSOs within successive contours of ^{13}CO line emission. We find a break in the relation between Σ_{SFR} and Σ_{gas}, with the relation being a power law ($\Sigma_{SFR} \propto \Sigma_{gas}^N$) with the index N varying between 1.4 and 3.6 above the break. The Σ_{gas} at the break is between 150–360 $M_\odot\,pc^{-2}$ for the sample clouds, which compares well with the threshold gas density found in recent studies of Galactic star-forming regions. Our clouds treated as a whole lie between the Kennicutt relation and the linear relation for Galactic and extra-galactic dense star-forming regions. We find a tendency for the high-mass YSOs to be found preferentially in dense regions at densities higher than 1200 $M_\odot\,pc^{-2}$ ($\sim$0.25 g cm^{-2}).

Key words: H II regions – ISM: clouds – stars: formation

Supporting material: machine-readable table

1. Introduction

Knowledge of the physical processes driving the conversion of interstellar gas into stars is fundamental to the development of a predictive physical theory of star formation. A basic step in this direction is to obtain empirical relations between parameters that are related to star formation. Schmidt (1959) suggested a relation between the star-formation rate (SFR) and the density of the gas, which in recent decades has been reformulated by Kennicutt (1998) as a relation between SFR surface density (Σ_{SFR}) and the surface density of the gas (Σ_{gas}). This relation, often referred to as Kennicutt–Schmidt (KS) relation, has a power-law form $\Sigma_{SFR} \propto \Sigma_{gas}^N$ with the index $N = 1.4$. The relation was established over kiloparsec (kpc) scales, using the HI and CO lines to trace the gas content and holds over more than four orders of magnitude in Σ_{gas}. The sampled regions encompass low-density gas in disks of galaxies as well as high-density gas in the infrared-bright circumnuclear regions.

Stars form predominantly in dense clumps, of sizes of about one parsec. These clumps themselves form part of larger molecular clouds (MCs). The CO line is the most commonly used tracer of the MC mass. However, it is a poor tracer of the high-density gas that resides in clumps. The denser regions are traced by high-density molecular lines such as NH$_3$ or by mapping the dust continuum submillimeter emission (Heyer et al. 2016). Gao & Solomon (2004) found a linear relation between SFR and the total mass of dense gas in luminous infrared galaxies. The nonlinear KS relation and the linear relation between the SFR and the mass of the dense gas, jointly imply an increase in the fraction of total gas in dense form as $\sim\Sigma_{gas}^{0.4}$ (Heiderman et al. 2010). Systems with very high SFRs, such as ultraluminous galaxies, have almost 100% of their gas in the star-forming dense phase, whereas at lower

SFRs, this fraction can be as small as 1% (Kennicutt & Evans 2012).

In recent years, the relation between the SF and gas mass has been explored at the scale of clumps and down to core scale in Galactic star-forming regions (e.g., Heiderman et al. 2010; Lada et al. 2010) using extinction maps at infrared (IR) wavelengths and/or dense gas tracers, to estimate the Σ_{gas}, and number counts of Young Stellar Objects (YSOs) along with a mean value of stellar mass per YSO and lifetime of Class II phase to estimate the SFR. These studies found a linear relations, much like the relation found by Gao & Solomon (2004) using dense gas tracers in luminous external galaxies. Additionally, Wu et al. (2010) and Heyer et al. (2016) have found linear relationships for dense clumps using dense gas tracers. Indeed, Heyer et al. (2016) found for dense clumps a strong linear correlation between Σ_{SFR} and Σ_{gas} normalized by free-fall and clump crossing times, suggesting the star formation is regulated at local scales. Heiderman et al. (2010) found that the linear relation holds above a threshold gas density of $\Sigma_{th} = 129\,M_\odot\,pc^{-2}$. For densities below the threshold Σ_{th}, the SFR drops steeply with a power index N as large as 4.6. Heiderman et al. (2010) also found that the SFR at a given Σ_{gas} in Galactic star-forming regions lies above the KS-derived SFR by factors of up to 17. They argued that this difference might arise due to the kiloparsec-size beams used to determine Σ_{gas} in extra-galactic studies, which mostly contains non-star-forming diffuse CO gas below Σ_{th}. Recent simulations by Calzetti et al. (2012) on the effects of sampling scale on the KS law support this idea.

Galactic studies that obtained a linear relation between the SFR and the gas density, have restricted their analysis to clumps, that are expected to transform almost all their mass into stars. Typical MCs contain gas at a variety of column densities, covering the entire range of Σ_{gas} found in extra-galactic studies,

with the clumps representing the high-end of the Σ_{gas} distribution. Hence, the star-formation law can be studied locally within individual MCs. Indeed, the original conjecture of Schmidt (1959) pertains to SF law within the clouds that are actively forming stars (Lada et al. 2013). Gutermuth et al. (2011) studied eight nearby low-mass star-forming clouds, and found a power-law relation with N ranging between 1.37–3.8. Lada et al. (2013) carried out a similar study for a sample of four nearby clouds, finding $N = 2.04$ for Orion A, Taurus, and California and $N = 3.3$ for Orion B. More recently, Willis et al. (2015) studied six massive star-forming clouds, finding an average slope of $N = 2.15 \pm 0.41$. They also found that the dispersion of the relationship within individual clouds is much lower than the differences in the N values from one cloud to another.

In summary, the value of N within star-forming Galactic MCs varies more than the range of values found for extra-galactic star-forming regions (Bigiel et al. 2008; Kennicutt & Evans 2012). In other words, there is no preferred value of N within MCs. Lada et al. (2013) have pointed out that even clouds having similar N values could have vastly different levels of star-formation activity because the latter depends on the density structure within clouds, which is found to vary significantly from cloud to cloud. Similar conclusions were drawn by Burkert & Hartmann (2013) using an analysis of the surface density structure within the Galactic star-forming clouds.

In the present study, we derive star-formation laws for high-mass star-forming MCs at sub-parsec- to parsec-scale spatial resolutions. Our approach differs from most previous explorations of this relationship for the Galactic MCs in three aspects: (1) the chosen MCs do not have a known optical nebula associated to them, indicating that SF activity has started recently in our sample of clouds. This ensures that the physical condition of the gas has not been altered by a previous generation of high-mass stars; (2) the chosen MCs contain at least one high-mass YSO, an IRAS source, which ensures that our MCs are high-mass star-forming regions, and (3) we use ^{13}CO data, instead of extinction maps, to derive the gas density. This procedure allows the exploration of embedded SF, even at relatively low surface densities. Our approach also allows us to quantify the difference in SFRs at a given Σ_{gas} between Galactic and extra-galactic studies, that used the same tracer, namely CO.

In this work, we carry out a search for Young Stellar Objects (YSOs) in the MCs associated with 12 IRAS sources at distances from 1 kpc to 5 kpc. In Section 2, we discuss the criteria for sample selection, and the method we have followed for defining the MCs associated with the IRAS sources. The sample of YSOs is discussed in Section 3, and, in Section 4, the mass function (MF) is presented. A detailed analysis of the star-formation law for the sample of star-forming regions is reported in Section 5. Our conclusions are summarized in Section 6.

2. The Sample and Observational Data

Our star-forming MCs for the study of the YSO population were selected using the following criteria: (a) they contain an IRAS source with characteristics of an ultra-compact H II region (Wood & Churchwell 1989), (b) the IRAS sources are associated with the dense cores detected by CS(2–1) line emission Bronfman et al. (1996), (c) the line of sight (LOS) for each cloud is devoid of any other foreground molecular

component associated to other MCs as inferred by the ^{13}CO (J = 1-0) spectra, and (d) they have GLIMPSE (Churchwell et al. 2009) and 24 μm-MIPSGAL (Rieke et al. 2004) Spitzer public data. The first two criteria ensure that the selected clouds contain high-mass star-formation sites. The third criterion is imposed to guarantee that all the YSOs associated geometrically to an MC are physically associated with it. The last criterion is the basis for the identification of the YSOs. Eighty clouds of the first quadrant of the Galaxy satisfied the first 2 criteria. However, the third criterion was satisfied by only 12 of these clouds, thus restricting our sample size to 12 MCs. All of these have GLIMPSE and MIPSGAL public data available. Typical Spitzer RGB images (3.6 μm, 8.0 μm, and 24 μm) of the resulting sample of clouds are shown in Figure 1, where the position of the IRAS source is identified by a cross symbol. Table 1 lists the properties of the IRAS sources compiled from the literature such as IRAS name, galactic coordinates, bolometric luminosities, distance to the object, etc.

2.1. Definition of the MC Associated with an IRAS Source

In order to define the parent molecular cloud that harbors the high-mass star-forming regions, we used ^{13}CO(J = 1-0) emission data from the Galactic Ring Survey (GRS) database (Jackson et al. 2006). The survey data have a velocity resolution of 0.21 km s^{-1}, a typical (1σ) rms sensitivity of ~0.13 K, a main beam efficiency of $\eta_{mb} = 0.48$, and a beam of 46$''$ (Jackson et al. 2006). The ^{13}CO emission spectra for the line of sight (LOS) to the selected IRAS sources are shown in Figure 2, where the observed velocity of the CS(J = 2–1) emission line (Bronfman et al. 1996) is marked with a dashed vertical line. In the inset, we show the results of a Gaussian fit to the observed ^{13}CO profile. The best-fitting value of the central velocity and the ^{13}CO line width (full width at half maximum—FWHM or ΔV) are given in the last column of Table 1. In the majority of the cases (10/12), there is a peak in ^{13}CO spectra within $\lesssim 3$ km s^{-1} with respect to the CS velocity, whereas in the two clouds (MC9 and MC21) the difference is ~7 km s^{-1}. Nevertheless in all clouds the difference between the ^{13}CO and the CS velocities is less than the FWHM of the fitted ^{13}CO profile. This association guarantees the coexistence of dense cores traced by the CS line with the dense molecular structures traced by the ^{13}CO line. All clouds are located in the first quadrant, where the foreground molecular emission, if present, would have produced a prominent ($>3\sigma$) molecular component to the left of the CS velocities in the plotted spectra. We could verify the absence of such a prominent component in 11 out of our 12 clouds, thus ensuring that the selected cloud is the nearest cloud along the LOS. The exception is MC81, whose CS velocity lies at the lower extreme of the velocity range covered by the GRS, which prevents us to infer the presence/absence of foreground molecular clouds. In this particular case, we used the ^{12}CO emission profile (see Figures 1 and 2 in Clemens et al. 1986; Dame et al. 2001, respectively) to ensure the absence of foreground molecular clouds along the LOS. For each MC, the integrated ^{13}CO emission map was created by summing at each pixel all channels that have a velocity within 15 km s^{-1} of the V_{peak}^{13CO}, and intensities $>3\sigma$.

The resulting column density map is shown by contours superposed on the RGB image in Figure 1. Only the portion of the map that has a molecular gas column density above $N_{H_2} \approx 1 \times 10^{21}$ cm^{-2} (the lowest plotted contour in Figure 1) is
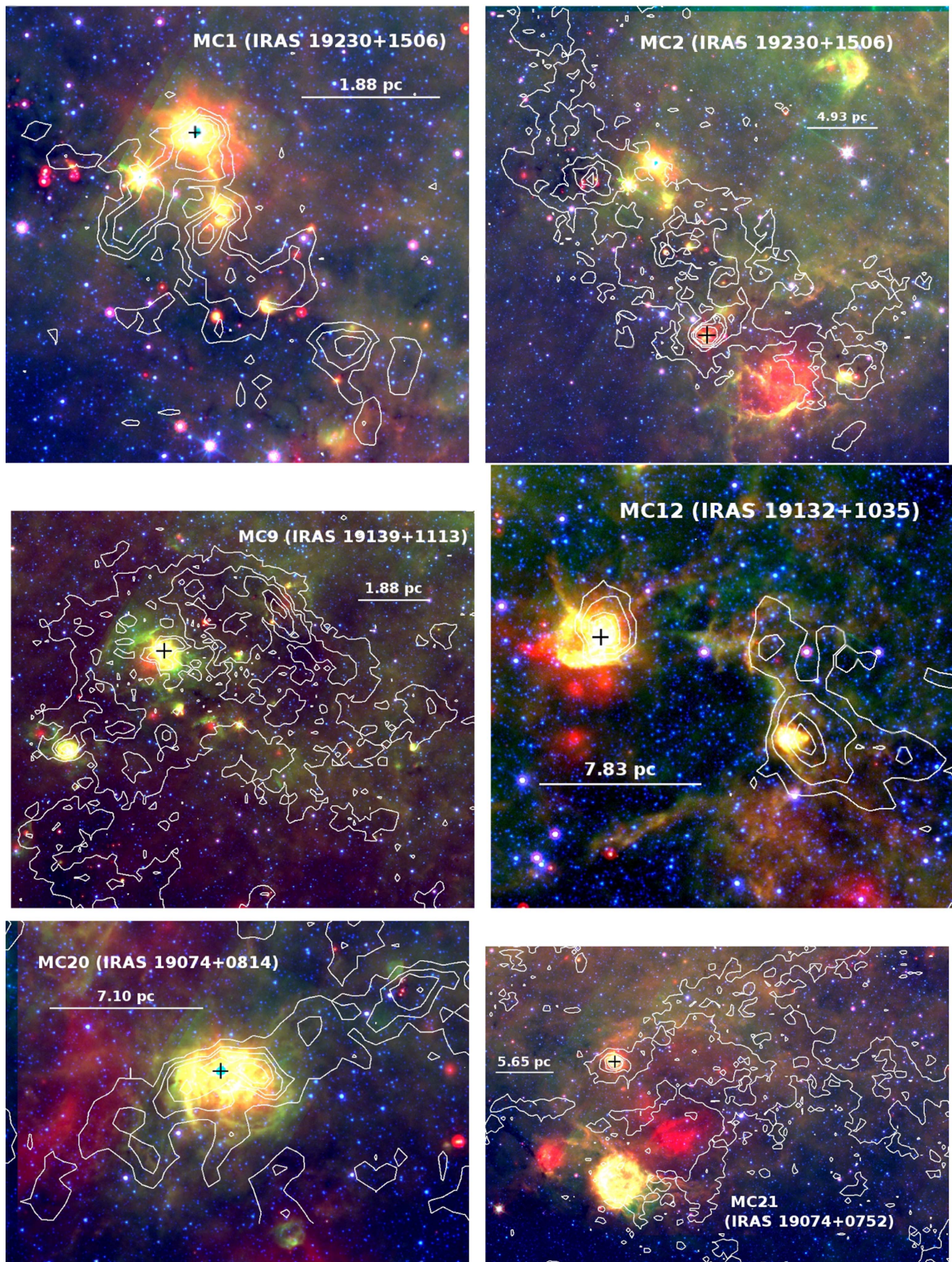
Figure 1. Color composite RGB image of our sample of molecular clouds using Spitzer 24 μm (R), 8 μm (G), and 3.6 μm (B) bands. The velocity-integrated ^{13}CO column densities are given in contours, with the lowest level corresponding to $N(H_2) = 1 \times 10^{21}$ cm^{-2} ($A_V \approx 1.0$ mag) and successive levels increasing in steps of 5×10^{21} cm^{-2}. The IRAS source position is marked with the cross symbol. The scale bar corresponding to $5'$ is shown as a horizontal bar.

considered part of the MC associated to the star-forming region. This limiting value corresponds to $A_V \sim 1$ mag, which is the value used in the literature as a physical threshold value to define

MCs (Bolatto et al. 2013). We complemented our ^{13}CO maps with the ^{12}CO emission integrated maps of Sanders et al. (1986) to obtain N_{H_2}, and thereby, the mass of the clouds.
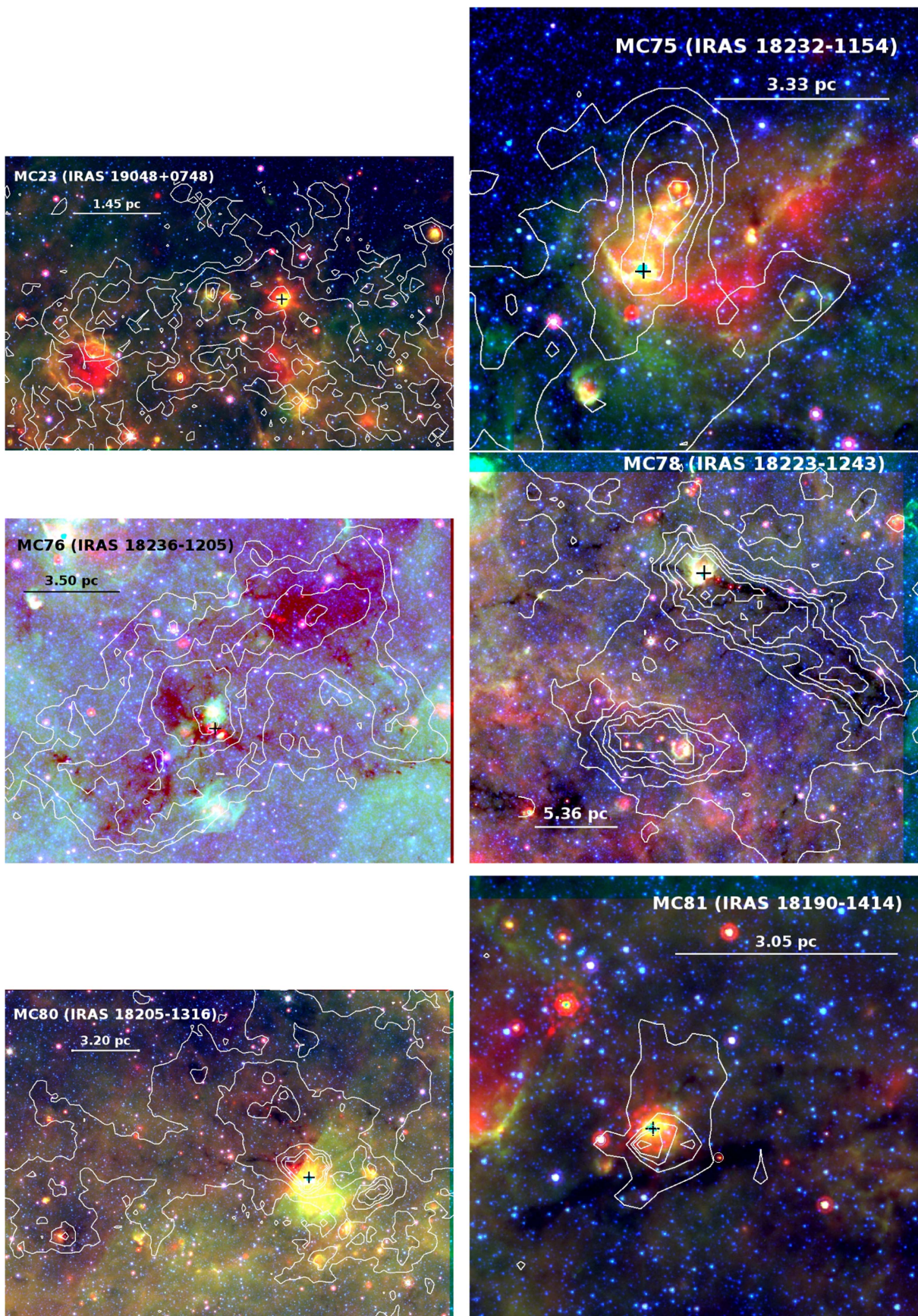
Figure 1. (Continued.)

Table 1
General Properties of MCs Associated with IRAS Sources with UCHII Colors

GMC	IRAS Name	Lon (°)	Lat (°)	Field size ($' \times '$)	L_{IRAS} ($10^3 L_\odot$)	$V_{\mathrm{LSR}}^{\mathrm{CS}}$ (ΔV) (km s^{-1})	D (kpc)	Scale (pc/$'$)	Area (pc^2)	^{13}CO Beam (pc)	$V_{^{13}\mathrm{CO}}^{\mathrm{peak}}$ (ΔV) (km s^{-1})
(1)	(2)	(3)	(4)	(5)	(6)	(7)	(8)	(9)	(10)	(11)	(12)
MC1	19230+1506	50.28	−0.39	15 × 15	4.2 (1.2)	16.6 (3.7)	1.3 (0.2)	0.38	23	0.29	14.5 (3.6)
MC2	19236+1456	50.22	−0.61	30 × 36	6.1 (1.8)	40.6 (4.5)	3.4 (0.4)	0.98	290	0.75	42.0 (8.6)
MC9	19139+1113	45.82	−0.28	30 × 24	40.3 (13.5)	50.8 (4.9)	4.8 (0.6)	1.38	59	0.29	58.2 (9.5)
MC12	19132+1035	45.19	−0.44	18 × 12	21.1 (6.8)	66.7 (2.2)	5.4 (0.6)	1.57	92	1.20	66.0 (5.1)
MC20	19074+0814	42.43	−0.26	15 × 9	65.1 (20.3)	65.6 (5.0)	4.9 (0.6)	1.42	57	1.09	65.0 (7.8)
MC21	19074+0752	42.11	−0.44	36 × 27	15.6 (4.6)	54.8 (3.0)	3.9 (0.5)	1.13	386	0.87	60.0 (10.7)
MC23	19048+0748	41.75	0.09	27 × 12	0.7 (0.2)	13.2 (2.4)	1.0 (0.1)	0.29	17	0.22	16.5 (4.7)
MC75	18232−1154	19.49	0.15	9 × 12	16.8 (5.2)	24.1 (4.0)	2.3 (0.3)	0.67	55	0.51	21.5 (8.0)
MC76	18236−1205	19.36	−0.02	25 × 12	7.0 (2.1)	25.9 (7.6)	2.5 (0.3)	0.70	82	0.54	26.0 (4.8)
MC78	18223−1243	18.66	−0.06	27 × 24	22.2 (6.8)	45.5 (2.9)	3.7 (0.4)	1.07	262	0.82	45.0 (3.4)
MC80	18205−1316	17.96	0.08	36 × 24	1.3 (0.4)	21.8 (2.8)	2.2 (0.3)	0.64	171	0.49	23.0 (5.7)
MC81	18190−1414	16.94	−0.07	6 × 9	5.4 (1.9)	−3.9 (2.7)	2.1 (0.3)	0.61	15	0.47	−4.1 (3.5)

Note. Brief explanation of columns: (1) the name of the molecular cloud containing the IRAS source; (2) name of the IRAS source; (3–4) Galactic longitude and latitude in degree; (5) approximate angular size of the clouds; (6) bolometric luminosity and their error based on distance of the IRAS source using the flux from the IRAS-PSC (http://irsa.ipac.caltech.edu/Missions/iras.html); (7) velocity with respect to the Local Standard of Rest of the CS source and their ΔV from Bronfman et al. (1996); (8) kinematical distance (with a percent error of 12%) to the dense clump associate with the IRAS source from Faúndez et al. (2004); (9) physical scale in parsec for an angular scale of $1'$; (10) physical area of the cloud above a column density of gas equivalent to $A_V = 1$ mag; (11) physical size of the $46''$ ^{13}CO beam at the distance of the cloud; and (12) peak velocity of the ^{13}CO and their line width obtained in this work.

2.2. Molecular Cloud Mass Estimation

We computed the mass of the clouds of the sample using three independent methods: (a) the virial theorem, (b) the local thermodynamical equilibrium (LTE) approximation, and (c) a constant conversion factor between CO and H_2 column density or an X-factor. To calculate the virial mass (M_{vir}) of the MC sample, we use the expression (May et al. 1997),

$$\left[\frac{M_{\mathrm{vir}}}{10^4 M_\odot}\right] = 1.58 \times \left[\frac{R_e}{5\,\mathrm{pc}}\right] \times \left[\frac{\Delta V}{5\,\mathrm{km\,s}^{-1}}\right]^2, \qquad (1)$$

where ΔV^{13} is the ^{13}CO line width (full width at half maximum—FWHM) obtained from a Gaussian fit to the observed spectra, R_e is the effective radius obtained from $R_e = \sqrt{A/\pi}$, where A is the area of the cloud. The expression assumes spherical symmetry in density (ρ), with $\rho \propto r^{-2}$ (MacLaren et al. 1988).

The LTE mass (M_{LTE}) is obtained from the ^{13}CO column density using the expression (Simon et al. 2001),

$$\left[\frac{M_{\mathrm{LTE}}}{10^4 M_\odot}\right] = 3.25 \times \left[\frac{R_e}{5\,\mathrm{pc}}\right]^2 \times \left[\frac{N(^{13}\mathrm{CO})}{10^{17}\,\mathrm{cm}^{-2}}\right], \qquad (2)$$

where $N(^{13}\mathrm{CO})$ is obtained by integrating the ^{13}CO column density at each pixel. To obtain the ^{13}CO column density map, we first obtained an excitation temperature for the cloud following the LTE approximation of Dickman (1978) and using the peak ^{12}CO radiation temperature from the published b–V maps from Sanders et al. (1986) in the corresponding longitude range and assumed that computed excitation temperature to be the same for all pixels in the ^{13}CO map. The coupling between beams and antenna efficiencies of ^{12}CO and ^{13}CO were taken into account.

A third method for the determination of the molecular mass consists of using the X-factor (XF). This factor is defined as the ratio between the column density of the molecular hydrogen ($N_{\mathrm{H_2}}$) and the CO luminosity $W(^{12}\mathrm{CO})$ (XF $\equiv N(\mathrm{H_2})/W(^{12}\mathrm{CO})$;

Pineda et al. 2008). In order to compare with previous results of Galactic studies on the Schmidt Law (Heiderman et al. 2010), we adopted the value of XF = $2.8 \pm 0.7 \times 10^{20}$ [cm^{-2} K^{-1} km^{-1} s] from Bloemen et al. (1986). Following Goto et al. (2003), we assumed $W(^{12}\mathrm{CO})/W(^{13}\mathrm{CO}) = 57$, resulting in the following expression for the column density of $N_{\mathrm{H_2}}$:

$$\left[\frac{N(\mathrm{H_2})}{\mathrm{cm}^{-2}}\right] = 57 \times 2.8 \times 10^{20} \times W(^{13}\mathrm{CO}). \qquad (3)$$

The molecular cloud mass (M_{XF}) is then calculated using the equation,

$$\left[\frac{M_{\mathrm{XF}}}{10^4 M_\odot}\right] = 3.26 \times \left[\frac{R_e}{5\,\mathrm{pc}}\right]^2 \times \left[\frac{W(^{13}\mathrm{CO})}{5\,\mathrm{K\,km\,s}^{-1}}\right]. \qquad (4)$$

All of the above equations are re-written from the original references by normalizing the quantities to their typical values in our MCs. The computed masses and other physical quantities of the clouds are listed in Table 2. The errors on the tabulated physical quantities are calculated by propagating the errors on R_e due to distance, ΔV, and $N(^{13}\mathrm{CO})$.

3. Identification of YSOs Associated to the Molecular Clouds

We used the sources from GLIMPSE and MIPSGAL programs of the Spitzer[1] Space mission to identify the YSOs in our sample of MCs. GLIMPSE sources are directly extracted from the GLIMPSE PSC catalog (Benjamin et al. 2003). We selected only those objects in the PSC that have detectable emission in all four of the GLIMPSE bands. MIPSGAL PSC (Gutermuth & Heyer 2015) was not available at the time when we started this work. We extracted MIPSGAL sources using the 24 μm images[2] (Carey et al. 2009) following the method described in the next subsection. The GLIMPSE and

---

[1] Spitzer Space Mission: http://www.spitzer.caltech.edu/.
[2] The BCD MIPSGAL images are provided by MIPSGAL survey online database, http://irsa.ipac.caltech.edu/data/SPITZER/MIPSGAL/.
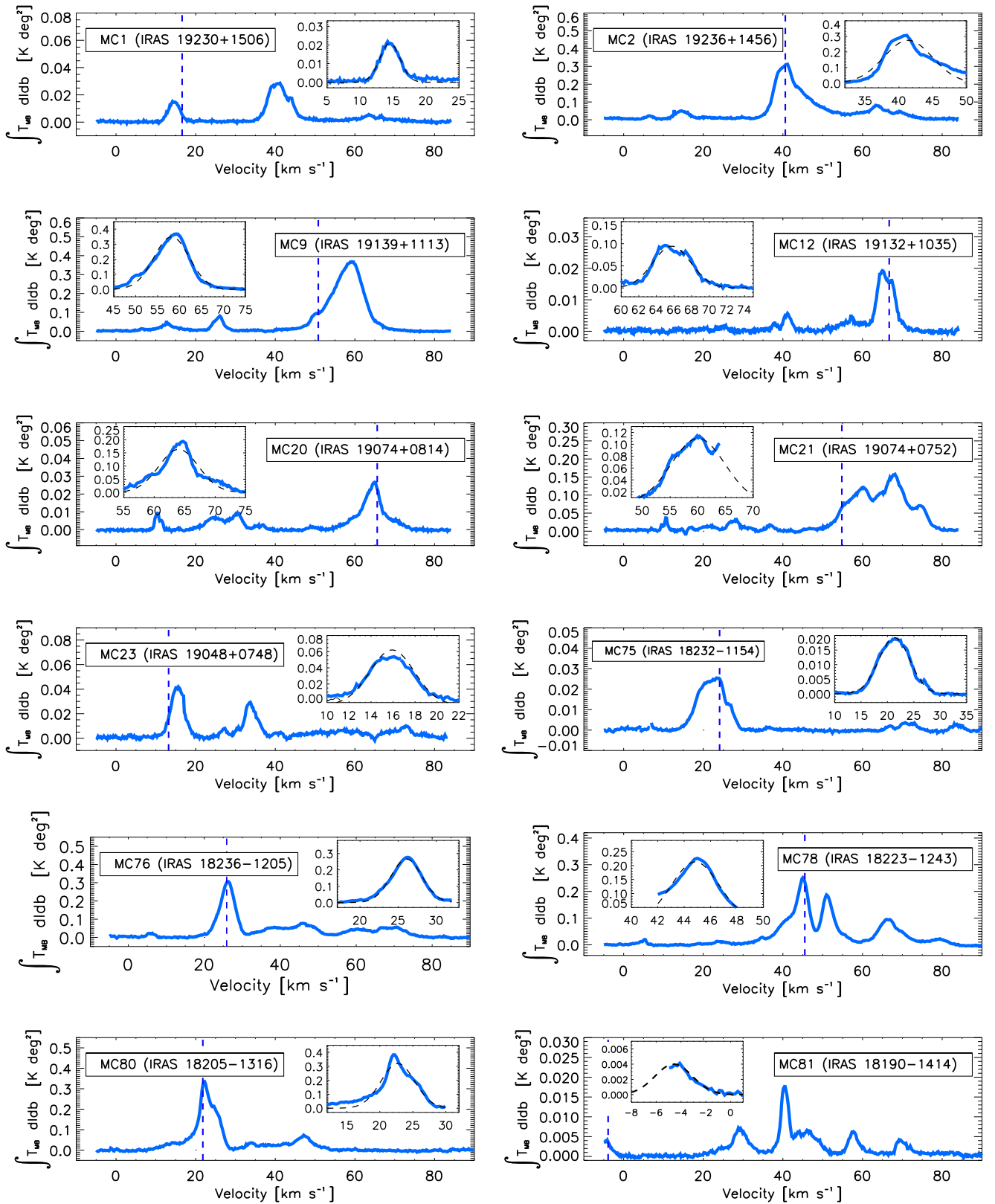
Figure 2. Line-of-sight ^{13}CO spectra from the GRS data cube integrated over the field of view (see column 5 in Table 1) of each molecular cloud. The vertical dashed line corresponds to the CS velocity from Bronfman et al. (1996). The Gaussian fit to the ^{13}CO profile is shown in the inset with a dashed black line. The ^{13}CO peak velocity and line width values obtained from the fit are listed in column 12 of Table 1.

MIPSGAL sources are merged to form a complete catalog of all YSOs. Any GLIMPSE source that is within the beam of FWHM = 6″ of the 24 μm image is considered a genuine counterpart of the 24 μm source. We aim to classify each detected YSO following the IR spectral index criterion of Lada (1987), see Section 3.4. The sensitivity of the MIPSGAL and

Table 2
Physical Properties of the Sample Molecular Clouds

GMC	N_{H_2} [10^{22} cm^{-2}]	A_V [mag]	M_{vir} [$10^4 M_\odot$]	M_{LTE} [$10^4 M_\odot$]	M_{XF} [$10^4 M_\odot$]
(1)	(2)	(3)	(4)	(5)	(6)
MC1	1.73 ± 0.77	18.40 ± 8.28	0.44 ± 0.38	0.33 ± 0.17	0.48 ± 0.26
MC2	1.28 ± 0.56	13.62 ± 6.13	8.87 ± 7.69	3.07 ± 1.55	4.50 ± 2.28
MC9	5.32 ± 2.39	56.61 ± 25.46	4.89 ± 4.21	2.56 ± 1.10	3.75 ± 1.89
MC12	2.95 ± 1.32	31.38 ± 14.12	1.75 ± 1.49	2.24 ± 1.12	3.28 ± 1.64
MC20	5.33 ± 2.39	56.70 ± 25.51	1.24 ± 2.82	2.44 ± 1.20	3.58 ± 1.78
MC21	1.10 ± 0.46	11.70 ± 5.26	16.06 ± 13.65	3.52 ± 1.59	5.17 ± 2.34
MC23	2.64 ± 1.18	28.08 ± 12.64	0.60 ± 0.53	0.30 ± 0.22	0.44 ± 0.32
MC75	5.05 ± 4.31	53.72 ± 24.16	3.37 ± 2.90	2.32 ± 1.20	3.39 ± 1.76
MC76	4.65 ± 2.09	49.46 ± 22.26	1.48 ± 1.30	3.14 ± 1.74	4.61 ± 2.54
MC78	6.28 ± 2.83	66.80 ± 30.06	1.34 ± 1.13	13.52 ± 6.46	19.84 ± 9.48
MC80	6.72 ± 3.02	71.49 ± 32.17	3.04 ± 2.61	9.57 ± 5.03	14.04 ± 7.38
MC81	1.80 ± 0.81	19.19 ± 8.62	0.35 ± 0.28	0.23 ± 0.11	0.34 ± 0.20

Note. Brief explanation of columns: (1) molecular cloud name; (2) molecular hydrogen column density determined from the ^{13}CO line; (3) visual extinction in mag equivalent to the derived gas column density; (4) cloud mass calculated using virial equilibrium (see Equation (1)); (5) cloud mass calculated using local thermodynamical equilibrium (see Equation (2)); and (6) cloud mass calculated using the X-factor (see Equation (4)).

GLIMPSE surveys ensures that our catalog contains all Class I sources of mass $\gtrsim 0.3\,M_\odot$, Class II sources more massive than $\sim 1\,M_\odot$, and Class III sources more massive than $\sim 5\,M_\odot$ for a cloud at an average distance of 3 kpc. These detection limits are obtained by converting the flux sensitivities (5σ corresponding to a point source) of GLIMPSE (Churchwell et al. 2005) and MIPSGAL[3] to bolometric luminosities at a distance of 3 kpc, and then using the Class-dependent luminosity to mass relation described in Section 4.2.1. It may be noted that most of the bolometric luminosity of Class I sources in their very early phase is outside the GLIMPSE bands. These sources, are expected to be the brightest ones at 24 μm. Thus, the addition of MIPSGAL sources allows us to select the high-mass tail of the mass function, as will be discussed in Section 4.

3.1. Identification of 24 μm YSO Candidates

We used *SExtractor* (Bertin & Arnouts 1996) on the 24 μm images to detect all sources that have S/N $\geqslant$ 5/pixel within the previously defined boundaries of the MCs. The *IRAF/phot*[4] task was used to obtain the photometric magnitudes of the selected sources. We carried out aperture photometry of the *SExtractor*-selected point sources using an aperture radius of 5 pixels (1 pix = 1″25 and FWHM of 24 μm MIPSGAL is 6″), and the sky annulus of inner radius of 18 pixels with a width of 5 pixels. The measured fluxes are corrected for the flux outside the aperture (infinite aperture correction) using a correction factor of 8.44 (average factor in all MIPSGAL images). Vega flux of 7.14 Jy as suggested in the MIPSGAL Data Handbook (Version 3.3) was used to convert the instrumental magnitudes to the 24 μm magnitudes. These sources are listed in column 2 of the Table 3.

The *SExtractor*-selected source list is contaminated by sources such as foreground stars (bright main sequence and AGB) and background objects (galaxies and highly reddened main-sequence stars). Use of bright 24 μm sources, where the infrared excess is more than two orders of magnitude above the photospheric

emission, relatively small sizes ($\lesssim 30'$) of our sample clouds, and the high column density toward the molecular clouds, minimizes the fraction of contaminating sources in our catalog. Nevertheless, we applied a Mid-Infrared (MIR) photometric filter to reject contaminating sources from our catalog.

3.2. 24 μm Sources without GLIMPSE Counterpart

Some of the 24 μm sources do not have a GLIMPSE counterpart. Genuine Class 0 and transitional Class 0/I sources are expected to be of this kind (André et al. 2010). However, the absence of a GLIMPSE counterpart does not necessarily mean the absence of emission in the 3–8 μm region. Sources could be missed in the GLIMPSE data set due to the problems with the photometry in any/some band(s) of GLIMPSE due to crowding or (bright) diffuse emission in the band. The brightest of such sources are expected to be detected in the NIR by the 2MASS.[5] In order to identify these bright reddened main-sequence stars, we performed a positional cross-match of the MIPSGAL sources with the 2MASS point-source catalog. All of these 2MASS-detected objects that satisfy the photometric color criteria of reddened main-sequence stars ($(J − H) \geqslant 1.75 \times (H − K)$), with the main-sequence as defined by Bessell & Brett (1988), were removed from the sample. In column 6 of the Table 3 the MS stars found in each cloud are listed. The sources without 2MASS counterparts, or with $(J − H) \leqslant 1.75 \times (H − K)$ and $(H − K)$ color excess, are considered genuine Class 0/I YSOs. These sources are listed in the column 3 of the Table 5 as Class 0 YSOs and are included in the final YSO selection (Section 3.3). However, a few of these sources could be highly embedded Class II YSOs in the high-density regions of the molecular clouds (Megeath et al. 2012).

3.3. Selection Criteria of YSOs

In order to identify the candidates to YSOs from the 24 μm detected sources, we used filters formed from a combination of GLIMPSE and MIPSGAL 24 μm colors as defined by Gutermuth et al. (2009). As a primary step, all GLIMPSE

---

[3] MIPS Instrument Handbook version 3: https://irsa.ipac.caltech.edu/data/SPITZER/docs/mips/mipsinstrumenthandbook/MIPS_Instrument_Handbook.pdf.

[4] IRAF is distributed by the NAAO, which is operated by the Association of Universities for Research in Astronomy Inc.

[5] Two Micron All Sky Survey (2MASS): http://irsa.ipac.caltech.edu/Missions/2mass.html.

Table 3
Selected MIPSGAL YSOs in Our Sample of MCs

GMC (1)	MIPSGAL Sources (2)	Selected Sources (3)	Selected Sources (%) (4)	NC Sources (5)	MS 2MASS Sources (6)	HLYSOs Sources (7)
MC1	16	16	100	…	…	16
MC2	179	170	95 (5)	25	9	124
MC9	172	141	82 (18)	73	31	117
MC12	23	7	30 (70)	…	…	7
MC20	46	36	78 (22)	13	3	33
MC21	228	219	96 (4)	60	11	152
MC23	128	109	85 (15)	24	21	27
MC75	40	15	38 (62)	…	…	15
MC76	149	103	69 (31)	54	45	102
MC78	142	125	88 (12)	29	15	125
MC80	299	279	93 (7)	38	20	213
MC81	13	4	31 (69)	…	…	4
Avg	…	…	72 (28)	…	…	…
Median	…	…	82 (18)	…	…	…

Note. (1) ID cloud; (2) selected sources from MIPSGAL 24 μm image; (3) selected sources after MIR filter; and (4) percent of selected sources after MIR filter, in parenthesis is the percent of rejected sources. Sources without conterpart in GLIMPSE are shown in column 5. Main-sequence 2MASS stars are shown in column 6. The final list of YSOs candidates with $L_{bol} > L_\odot$ are shown in column 7.

sources from the PSC with photometric errors $\sigma < 0.2$ mag in all IRAC bands are selected. Foreground main-sequence objects are expected to be bluer than $[X] - [24] = 1.0$ mag (Gutermuth et al. 2009), where $[X]$ is the magnitude in the [4.5] and [5.8] bands. Such sources are also expected to have $[3.6] - [24] < 1.0$ mag, which is the selection criterion we used to reject all foreground main-sequence stars. Given the sensitivities of GLIMPSE and MIPSGAL images, all 24 μm sources without a GLIMPSE counterpart are redder than this criterion, and hence are genuine YSOs. Foreground AGBs are relatively bluer and brighter than YSOs—and have colors of $[3.6] - [8.0] < 1.5$ and $[8.0] < 6.0$ mag. (Marengo et al. 2008). The candidate sources that satisfied this criterion are removed from our sample. Given the relatively small field sizes and low Galactic latitudes of our sample sources, our sample of YSOs is not expected to be contaminated by background galaxies. In total, the rejected number of objects amounts to ~28% (average; see column 4, Table 3). All objects remaining after applying these filters are considered "bona fide" YSOs. These sources, including the Class 0 YSOs, their galactic coordinates (columns 2 and 3) and GLIMPSE and 24 μm MIPSGAL photometric magnitudes (columns 4–8) are listed in the Table 4.

3.4. Classification of YSOs

In order to characterize the YSOs and describe their nature, we have used the infrared spectral index (α) as was defined in early works by Lada & Wilking (1984) and Lada (1987). This index has been extensively used to study the nearby (<1 kpc), predominantly low-mass, star-forming regions (Hartmann et al. 2005; Harvey et al. 2006; Alcalá et al. 2008; Gutermuth et al. 2008). Though originally defined to describe the evolutionary phases of low-mass stars, the α index is applicable for high-mass YSOs as well (Deharveng et al. 2012; Ellerbroek et al. 2013; Saral et al. 2015). We defined α for each 24 μm-source using the GLIMPSE and MIPSGAL data that cover a wavelength range from 3.6 μm to 24 μm. We followed the often-used definition of Greene et al. (1994) to carry out the classification. According to this classification, YSOs are Class I

if $\alpha \geqslant -0.3$, Class II if $-1.6 \leqslant \alpha < -0.3$, and Class III if $\alpha < -1.6$. The sources without GLIMPSE counterpart (Class 0/I YSOs) are considered Class I and a spectral index of 0.35 is assigned to them. In the original definition of Greene et al. (1994) the YSOs with $-0.3 < \alpha < 0.3$ are classified as Class FLAT. In this work, we included these α-values into the Class I classification. The α-values as defined by Greene et al. (1994) requires 24 μm detection and hence we used the slightly less reliable photometric color criteria of Gutermuth et al. (2008) to classify GLIMPSE YSOs without MIPSGAL counterpart. For this sample, 12%–45% of the MIPSGAL sources are Class I with a median value of 22%, where the upper percentages are affected by the small statistics of YSOs in some clouds; whereas the fact that only 9%–31% (with a median value of 23%) is Class I YSOs in GLIMPSE sources. On the other hand, the majority of the GLIMPSE sources are Class II (20%–86%, with a median value of 77%). The classification of the YSOs are shown in column 9 of Table 4.

4. Mass of the YSOs

Having obtained a sample of YSOs, we now use their merged photometry in GLIMPSE and MIPSGAL data to obtain a mass function (MF). The first step for achieving this is to obtain the bolometric luminosities (L_{bol}) of the sample YSOs. Knowledge of class is crucial in determining the bolometric luminosity of embedded YSOs. Even so, detection at 24 μm is key for a reliable determination of L_{bol}, because the bolometric correction factor for GLIMPSE-only sources is highly uncertain.

4.1. Mass of the GLIMPSE Sources

The c2d Survey (Evans et al. 2003) is one of the legacy programs of the Spitzer Space Mission that has provided uniform photometric data in the IRAC and MIPS bands of Spitzer of YSOs in well-known nearby star-forming regions. These regions were part of follow-up studies at far-infrared (60 μm to 500 μm) by Herschel and submillimeter/millimeter by ground-based facilities such as SIMBA/SEST, SCUBA/JCMT, and MAMBO/IRAM.

Table 4
Photometric and Physical Properties of the YSOs

Name	Lon °	Lat °	[3.6] mag	e3.6 mag	[4.5] mag	e4.5 mag	[5.8] mag	e5.8 mag	[8.0] mag	e8.0 mag	[24] mag	e24 mag	C	β	L_{bol} $L_{\odot}$	Mass $M_{\odot}$	H
(1)	(2)	(3)	(4)	(5)	(6)	(7)	(8)	(9)	(10)	(11)	(12)	(13)	(14)	(15)	(16)	(17)	(18)
MC1-M1	50.26111	−0.49540	8.55	0.04	8.49	0.05	7.97	0.04	7.96	0.03	6.22	0.04	2	−2.2	0.33	1.5	0
MC1-M2	50.26936	−0.47162	14.87	0.14	13.19	0.12	11.67	0.10	10.91	0.05	7.68	0.10	2	−2.2	−0.26	1.0	0
MC1-M3	50.21999	−0.45542	12.50	0.18	12.50	0.18	5.28	0.03	5.32	0.02	5.15	0.03	3	−3.3	2.53	4.5	1
MC1-M4	50.32986	−0.44956	8.32	0.04	7.99	0.05	7.55	0.04	7.49	0.04	6.95	0.06	3	−3.3	1.81	3.0	1
MC1-M5	50.23466	−0.47592	12.45	0.07	12.23	0.09	12.05	0.18	12.50	0.18	7.22	0.07	1	−1.3	−0.07	1.0	0
MC1-M6	50.22746	−0.50346	13.51	0.07	13.18	0.10	12.50	0.18	12.50	0.18	7.05	0.07	1	−1.3	−0.01	1.0	0
MC1-M7	50.22213	−0.49915	12.93	0.07	12.17	0.07	11.65	0.10	10.95	0.10	4.04	0.02	1	−1.3	1.20	2.0	1
MC1-M8	50.23388	−0.47583	13.86	0.11	12.27	0.09	10.98	0.09	10.33	0.06	7.22	0.07	2	−2.2	0.71	1.5	0
MC1-M9	50.23447	−0.50454	14.39	0.13	12.69	0.11	11.88	0.10	11.17	0.07	8.07	0.12	1	−1.3	−0.41	0.9	0
MC1-M10	50.22111	−0.49915	12.80	0.07	12.18	0.08	11.51	0.10	11.14	0.13	4.04	0.02	1	−1.3	1.20	2.0	1
MC1-M11	50.22149	−0.49979	12.69	0.08	11.71	0.07	10.42	0.06	8.81	0.03	4.04	0.02	2	−2.2	1.98	3.0	1
MC1-M12	50.29696	−0.42889	12.50	0.18	6.65	0.06	6.25	0.03	6.08	0.03	5.09	0.03	1	−1.3	0.78	1.5	0
MC1-M13	50.30923	−0.42042	7.18	0.04	6.66	0.04	5.97	0.03	5.51	0.03	3.17	0.01	2	−2.2	2.33	4.0	1
MC1-M14	50.22479	−0.46537	13.01	0.06	11.48	0.07	10.38	0.06	9.51	0.03	4.98	0.03	1	−1.3	0.82	1.5	0
MC1-M15	50.25849	−0.50773	11.51	0.04	10.85	0.06	10.37	0.06	9.52	0.04	6.61	0.05	2	−2.2	0.95	1.5	0
MC1-M16	50.27218	−0.50201	11.54	0.15	11.09	0.13	12.50	0.18	12.50	0.18	3.59	0.01	3	−3.3	1.38	2.0	1

Note. Brief explanation of columns. (1) The name of the MIPSGAL/GLIMPSE YSO in the sample. The name includes two parts, the first part is the name of the cloud, and the second part starts with a letter M or G (M indicates detected in MIPSGAL, and G indicates detected only in GLIMPSE), followed by the source number. The GLIMPSE-only detected sources do not have 24 μm related quantities, and hence a place-holder value of −1.00 is assigned for these sources under columns 12–13 and 15–18. (2–3) Galactic longitude and latitude for the YSOs. (4–13) GLIMPSE and 24 μm-MIPSGAL photometric magnitudes and errors. (14) IR spectral classification of the YSOs. Numbers 0, 1, 2, and 3 stand for Classes 0, I, II, and III, respectively. (15) log β-values of the YSOs as defined in Section 3.4. (16–17) log(L_{bol}) and mass of the YSOs derivated as explained in Section 4.2. The errors on L_{bol} and mass are roughly 30%. (18) A flag indicating whether the YSO is of high luminosity: 1 for YSOs with $L_{bol} \geqslant 10\ L_{\odot}$, 0 otherwise.

(This table is available in its entirety in machine-readable form.)

YSOs in Gould's Belt (GB) also had been the target of multi-band surveys. Detailed analysis of the resulting spectral energy distributions (SEDs) extending from the MIR to millimeter wavelengths has allowed for the determination of stellar masses for individual YSOs. This in turn has allowed for the construction of the mass function of YSOs (e.g., Enoch et al. 2006; André et al. 2010). Most of these low-mass star-forming regions are consistent with a log-normal initial mass function (IMF) as defined by Chabrier (2003) with a characteristic mass of $0.5\,M_\odot$ (Kennicutt & Evans 2012). Following these studies, we assume a log-normal mass function for the low-luminosity YSOs, which are mainly GLIMPSE sources, and assign a mean YSO mass of $0.5\,M_\odot$ for each source in this population.

4.2. Mass of the 24 μm Detected Sources

4.2.1. Bolometric Luminosity

Stars are still embedded in the MC during their PMS phase. The material in the immediate vicinity of the star absorbs almost all of the radiation emitted from the PMS star, re-radiating it in the infrared, including at the 24 μm band. We define a quantity $\beta = L_{24}/L_{bol}$, where β is the fraction of the bolometric luminosity that is emitted in the 24 μm band. The emission at 24 μm arises from the warm circumstellar dust and depends on the dust temperature and the mass of the heated dust envelope. During the evolution from Class 0/I (protostars) to Class II (PMS object), the dust temperature of the circumstellar material is expected to increase due to the increase of the "photospheric" temperature, which would lead to an increase of the fraction β. The accretion of the envelope material to the disk also contributes to the increase of the dust temperature (Stahler & Palla 2005). However, the envelope mass decreases at a faster rate due to effects of outflows, radiative pressure, and stellar winds, with the net result being a decrease of β along the PMS phase. A detailed modeling of β variation is beyond the scope of this work. Hence, we looked for an empirical relation between β and the SED evolutionary phases of the YSOs using a recent complete IR plus submillimeter photometric data set for YSOs.

We used the YSOs from the c2d and GB recent data sets, that have both the 24 μm and bolometric luminosities cataloged, to obtain β empirically using the evolutionary Classes I–III. To start with, we classified the objects in these data sets into evolutionary SED Classes I, II, and III following the criteria of Greene et al. (1994). In Figure 3, we show the $\beta - L_{bol}$ diagram for the c2d+GB YSOs from Evans et al. (2003) and Dunham et al. (2015). This population is dominated by Class II YSOs (filled circles), though there is a considerable fraction of Class I (open circles) and Class III YSOs (triangle symbols). The Class I sources have the highest β-values, while the Classes II and III span values between 10^{-1} and 10^{-5}. The distribution of β values for each Class is shown as histogram in the right panel, where the peak values traced by dashed lines are used as typical values for each Class. These β-values are 5.6×10^{-2}, 6.0×10^{-3}, and 5.6×10^{-4}, for Classes I, II, and III, respectively.

For our embedded sources of Class 0/I, which are detected only in 24 μm, we used the relation $L_{bol} = 3.31 \times L_{MIR}$ of Kryukova et al. (2012) for a spectral index of 0.35. The mid-infrared luminosity, L_{MIR}, is the luminosity in the 1–24 μm range, which is calculated from the 24 μm flux (S_{24} in Jy) using
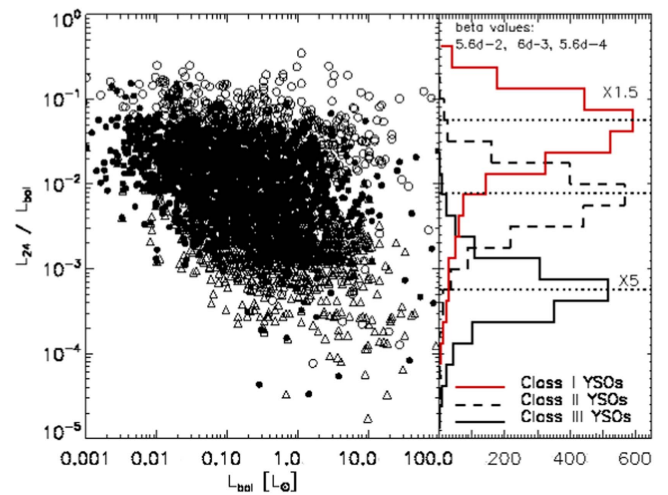
Figure 3. $\beta = L_{24}/L_{bol}$ vs. L_{bol} diagram for YSOs from c2d and GB data surveys (left). The Class III, Class II, and Class I YSOs are shown by triangles, filled circles, and open circles, respectively. The histograms to the right show the distribution of β for each Class, where the numbers in each Class are normalized to roughly match the number of Class II YSOs, by multiplying by factors 1.5 and 5 (denoted as X1.5 and X5). The median value of each distribution is shown by a dotted line and points out in the top of the panel, and it is used as a typical value for each Class.

the relation, $L_{MIR}/L_\odot = [0.05 + 0.81\,S_{24}] \times D^2$, where D is the distance to the cloud in kiloparsecs. For deriving the latter relation, we have substituted the flux terms in the 2MASS and GLIMPSE bands by the 3σ upper limits in these bands.

We constructed the bolometric luminosity function (LF) for all the 24 μm-detected YSOs of our sample using the β value corresponding to its Class. The resulting bolometric LFs for eight of our MCs that contain at least 20 luminous YSOs are shown in Figure 4. These are plotted separately for Class I (shaded area), Class 0/I (hatched area), and all YSOs. The median luminosities of MIPSGAL-selected Class I YSOs (vertical dotted line) in different clouds varies between 0.3–80 $L_\odot$, with a global median of ~8 $L_\odot$. It is interesting to note that the median luminosity for all sources (vertical dashed line) is higher than that for Class I YSOs in every cloud. This implies that the most luminous sources (and the most massive sources) in the MCs are systematically more evolved (Class II and III).

4.2.2. Luminosity–Mass Relation

Observed bolometric luminosity of an accreting star comes from three physical processes: (1) accretion, (2) nuclear burning, and (3) Kelvin–Helmholtz contraction. The contribution from the last two processes is well understood and is calculated theoretically in traditional PMS evolutionary tracks (Palla & Stahler 1993; Tognelli et al. 2011). For stars with masses $>1.5\,M_\odot$, the luminosity from accretion is not dominating the observed 24 μm flux, and the nuclear luminosity is a good approximation to the observed values (Hillenbrand & White 2004). For example, Myers (2014) obtain, depending on the model assumptions, accretion luminosities between 250–1500 $L_\odot$ for a protostar of 5 $M_\odot$, which is comparable to the 5 $M_\odot$ ZAMS value of ~800 $L_\odot$ from Tognelli et al. (2011).

However, the relative contribution of accretion to the total luminosity, for low-mass stars (mass $< 1\,M_\odot$) in their early
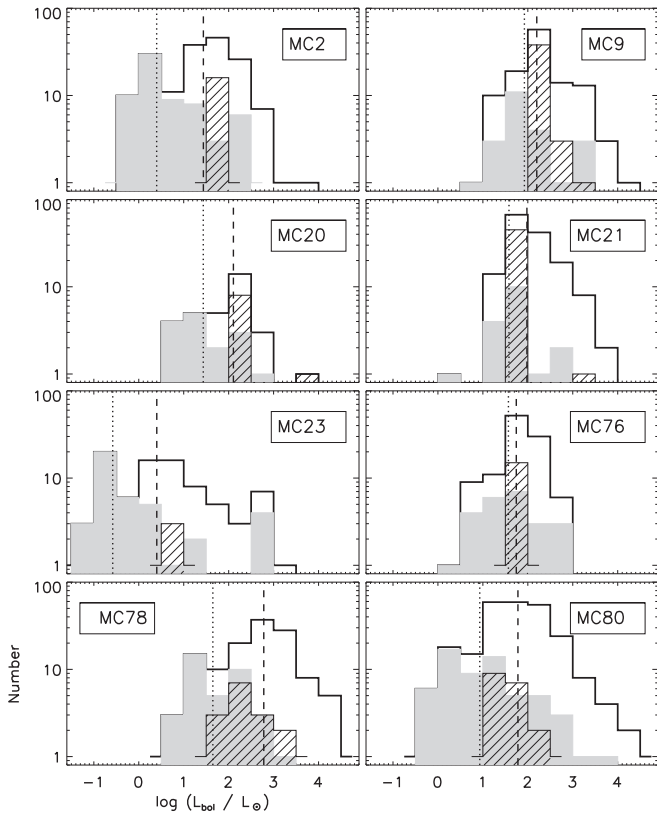
Figure 4. Bolometric Luminosity Function of MIPS-detected YSOs in 8 of our molecular clouds, separated by Class as indicated in the plot (All: solid histogram, Class I: shaded, Class 0/I: hatched). Median values for All (dashed) and Class I (dotted) YSOs are shown by vertical lines. Sources with $L_{bol} > 10\,L_\odot$ are considered as high-luminosity YSOs.

Class I stage is still under debate. In general, theoretically predicted accretion rates produce luminosities that are a factor of ~5 higher as compared to the median (observed) luminosity of accreting stars (Kenyon et al. 1990; Enoch et al. 2009). On the other hand, observations of high-luminosity variable sources, such as the prototype FU Ori, suggest that protostars undergo periods of high accretion, in events known as episodic accretion (e.g., Hartmann & Kenyon 1996; Vorobyov & Basu 2005). In the extreme case, protostars may spend most of their life in the low-luminosity, low-accretion phase and accrete most of their mass during short, intense accretion bursts. Even with episodic bursts of accretion, protostars need to find a way to lose as much as 75% of the accretion energy in non-radiative winds (Offner & McKee 2011).

The sensitivity of MIPSGAL at the distances of sample clouds corresponds to bolometric luminosity of ~1 $L_\odot$. The median bolometric luminosity of Class I YSOs of our sample is ~8 $L_\odot$, which is similar to the value given for GLIMPSE-selected YSOs of Offner & McKee (2011) but exceeds by a factor of five from Kennicutt & Evans (2012). On the other hand, 10 $L_\odot$ corresponds to the luminosity of a ~2 $M_\odot$ ZAMS star in models of Tognelli et al. (2011). The above discussions clearly illustrate that reliable masses could be obtained for luminous MIPSGAL Class I YSOs using PMS evolutionary tracks. For Class II and Class III sources, the accretion contribution is expected to be even less. Hence we determined the high-mass end of the mass function using Tognelli et al. (2011) PMS evolutionary tracks.

YSOs spend different timescales in each of the evolutionary Classes I, II, and III. The timescale in each of these phases depends on the stellar mass. These timescales have been studied in nearby star-forming regions in the c2d and GBS (Evans et al. 2009; Dunham et al. 2015). The values used in this work are 0.5 Myr and 2.0 Myr for Class I and Class II, reported by Kenyon & Hartmann (1995) and Evans et al. (2009), respectively. These values are around those obtained in recent works by Heiderman & Evans (2015) and Dunham et al. (2015), particularly the timescale for early Class I YSOs. For the Class III, a timescale of 3 Myr is used (though there are longer PMS timescales for low-mass stars).

In order to assign a mass to the bolometric luminosity of the YSOs, we have used the following procedure: (a) if the source is Class III, a mass from the PMS evolutionary track for 3 Myr is used, (b) if the source is Class II, we assign a mass from the evolutionary track for 2 Myr, while for Class I and Class 0/I YSOs, we assign a mass from the 0.5 Myr track.

Hereafter, we refer all YSOs satisfying $L_{bol} > 10\,L_\odot$ as high-luminosity sources (HLYSOs), with the rest of the sources, including the GLIMPSE-only detected YSOs referred to as low-luminosity sources (LLYSOs). In Table 5, we give the Class distribution and masses of HLYSOs and LLYSOs. In general, HLYSOs are dominated by Class I sources, whereas the Class II sources are the most frequent among LLYSOs. The mean mass of HLYSOs in different MCs ranges from 2 to 6.6 $M_\odot$, with a median value of 4 $M_\odot$ for the whole sample.

In Figure 5, we plot the fractions of Class I and Class II YSOs in high (top panel) and low (middle panel) luminosity samples for each MC. HLYSOs are predominantly Class I (63%), whereas LLYSOs are dominated by Class II (79%) sources. In the bottom panel, we show the contribution of HLYSOs to the total "stellar" mass for each MC. It can be noted that in eight of our MCs, these HLYSOs, which are systematically more massive than the LLYSOs (see the mean mass in the last two columns of Table 5), contribute more than 50% of the total "stellar" mass. For the total sample, 62% of the total mass is contributed by the HLYSOs.

4.3. The Mass Function of the YSOs

Observational determination of the mass function (MF) of YSOs is critical for a detailed understanding of star formation. Studies of nearby star-forming regions have by now established the nature of the MF of YSOs in the *c2d* and GB surveys (Enoch et al. 2006; André et al. 2010). Particularly, André et al. (2010) found that the protostellar core mass function significantly resembles the log-normal Stellar MF (Chabrier 2003), but with the characteristic mass ~3 times higher. It should be noted that the regions analyzed in these studies lack the high-mass star population, and hence the application of Chabrier function to star-forming regions containing high-mass stars, such as the regions studied in the present work, is still questionable. There is growing evidence that such regions have an excess of high-mass stars above the Chabrier function, which can be well represented by the Salpeter (1955) IMF (see the review by Bastian et al. 2010). We investigate here whether this is the case for the star-forming regions studied in the present work.

The method we have followed for the MIPSGAL sources to obtain the YSO masses allows us the construction of the high-mass end of the MF in all MCs. The resultant MFs are plotted

Table 5
Class and Mass Distribution of YSOs in Our Sample of MCs

|	High-luminosity					Low-luminosity					Stellar Mass			
GMC	CI	C0	CII	CIII	HLYSOs	CI	CII	CIII	LLYSOs	Total YSOs	HLYSOs $[M_\odot]$	LLYSOs $[M_\odot]$	HLYSOs $M_\odot/N$	LLYSOs $M_\odot/N$
(1)	(2)	(3)	(4)	(5)	(6)	(7)	(8)	(9)	(10)	(11)	(12)	(13)	(14)	(15)
MC2	17	16	71	15	119	74	352	11	437	556	440 ± 13	219 ± 5	3.7	0.5
MC9	22	42	21	32	117	93	633	18	744	861	630 ± 19	372 ± 5	5.4	0.5
MC20	11	10	6	2	29	40	211	12	263	292	144 ± 9	132 ± 3	4.9	0.5
MC21	17	46	30	59	152	49	448	23	520	672	665 ± 17	260 ± 5	4.4	0.5
MC23	6	3	14	4	27	162	398	5	565	592	102 ± 7	283 ± 5	3.8	0.5
MC76	19	15	57	8	99	121	433	13	567	666	371 ± 12	284 ± 5	3.7	0.5
MC78	33	14	11	61	121	149	435	16	600	721	795 ± 24	300 ± 5	6.6	0.5
MC80	29	18	52	112	211	118	325	7	450	661	882 ± 20	225 ± 5	4.2	0.5
MC1	7	0	3	2	12	14	91	13	118	130	25 ± 3	59 ± 3	2.0	0.5
MC12	2	0	1	4	7	51	106	6	163	170	28 ± 3	82 ± 3	3.5	0.5
MC75	5	0	4	5	14	131	428	23	582	596	62 ± 6	293 ± 5	4.6	0.5
MC81	1	0	1	2	4	3	2	5	10	14	13 ± 2	5 ± 1	3.3	0.5

Note. Brief explanation of columns. (1) GMC name. (2–6) Distribution of high-luminosity YSOs into Class I (CI), Class 0 (C0), Class II (CII), and Class III (CIII). The column labeled HLYSOs contains the total number of HLYSOs. (7–10) Distribution of low-luminosity YSOs into different Classes. The column labeled LLYSOs contains the total number of LLYSOs. (11) Total number of HL and LL YSOs. (12–13) Total mass of all high- and low-luminosity YSOs. (14–15) Mean mass of a high- and low-luminosity YSO; Data for the four MCs with less than 20 high-luminosity YSOs are given in the bottom four rows.
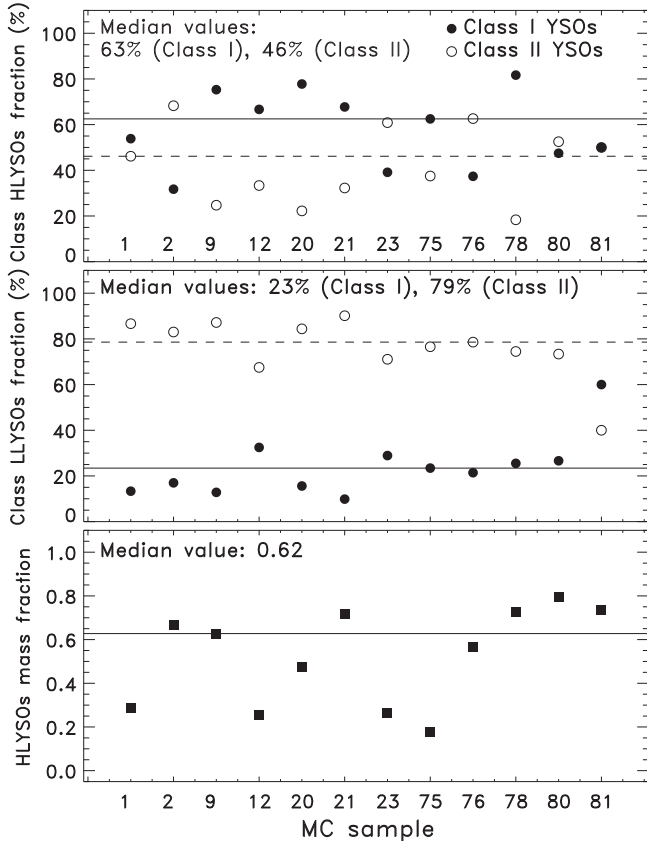
Figure 5. Relative fraction of Class I (filled circles) and Class II (open circles) YSOs among the high-luminosity (top) and low-luminosity (middle) sources in each MC identified by its number vertically below the symbol. HLYSOs are predominantly Class I, whereas LLYSOs are dominated by Class II sources. The horizontal lines give the median value for each Class (solid for Class I and dashed for Class II). The relative contribution of HLYSOs to the total mass in YSOs is shown in the bottom panel. In our sample of MCs, HLYSOs contribute between 20%–80% of the total mass, with the median value 63%.

in Figure 6 by solid histograms. The MFs are binned in logarithmic mass intervals of 0.3 dex. The error in the masses due to the unaccounted contribution of the accretion in deriving the YSO masses, would overestimate the masses at the most by one bin width. In Figure 6, we also show a log-normal Chabrier MF for the LLYSOs. This function is centered at a characteristic mass of $0.5 M_\odot$ and normalized in such a way that the total number above $0.1 M_\odot$ for the function is equivalent to the total number of observed LLYSOs in each cloud. The plotted Chabrier MF assumes that all the YSOs more massive than $0.1 M_\odot$ are detected in the GLIMPSE survey. For each MC, we show the sensitivity limit for Class I sources in the figure. It can be seen that almost all the Class I sources are indeed detected by GLIMPSE in our sample clouds. On the other hand, we may be missing the Class II sources with masses lower than g_{II}, the limiting GLIMPSE mass for Class II sources. In all cases, g_{II} is less than the characteristic mass, and hence in the extreme case, the actual numbers could be a factor of two higher than the detected YSOs.

Even after taking into account the possible error in the normalization of the Chabrier MF, the number of expected stars more massive than $3 M_\odot$ is less than 1 in our sample of MCs. Thus, the observed number of high-mass stars is clearly above those expected from the Chabrier MF in all clouds. On the other hand, the observed number of massive stars is consistent with a Salpeter IMF for stars more massive than $\sim 2 M_\odot$. That is shown in the Figure 7, where the mass function for the total YSO population of the cloud sample is plotted. In this figure, the mass distribution of the HLYSOs is shown with the histogram, while the dotted curve represents the mass distribution of the LLYSOs. An error weighted fit for the masses greater than $2 M_\odot$ is plotted with the dashed line, where the slope found ($\alpha = -1.4 \pm 0.4$) resembles the Salpeter index well ($\alpha = -1.3$). This hybrid Chabrier plus Salpeter mass function that we propose for our regions is in fact the favored MF in other regions with massive SFs (see the review by Bastian et al. 2010).
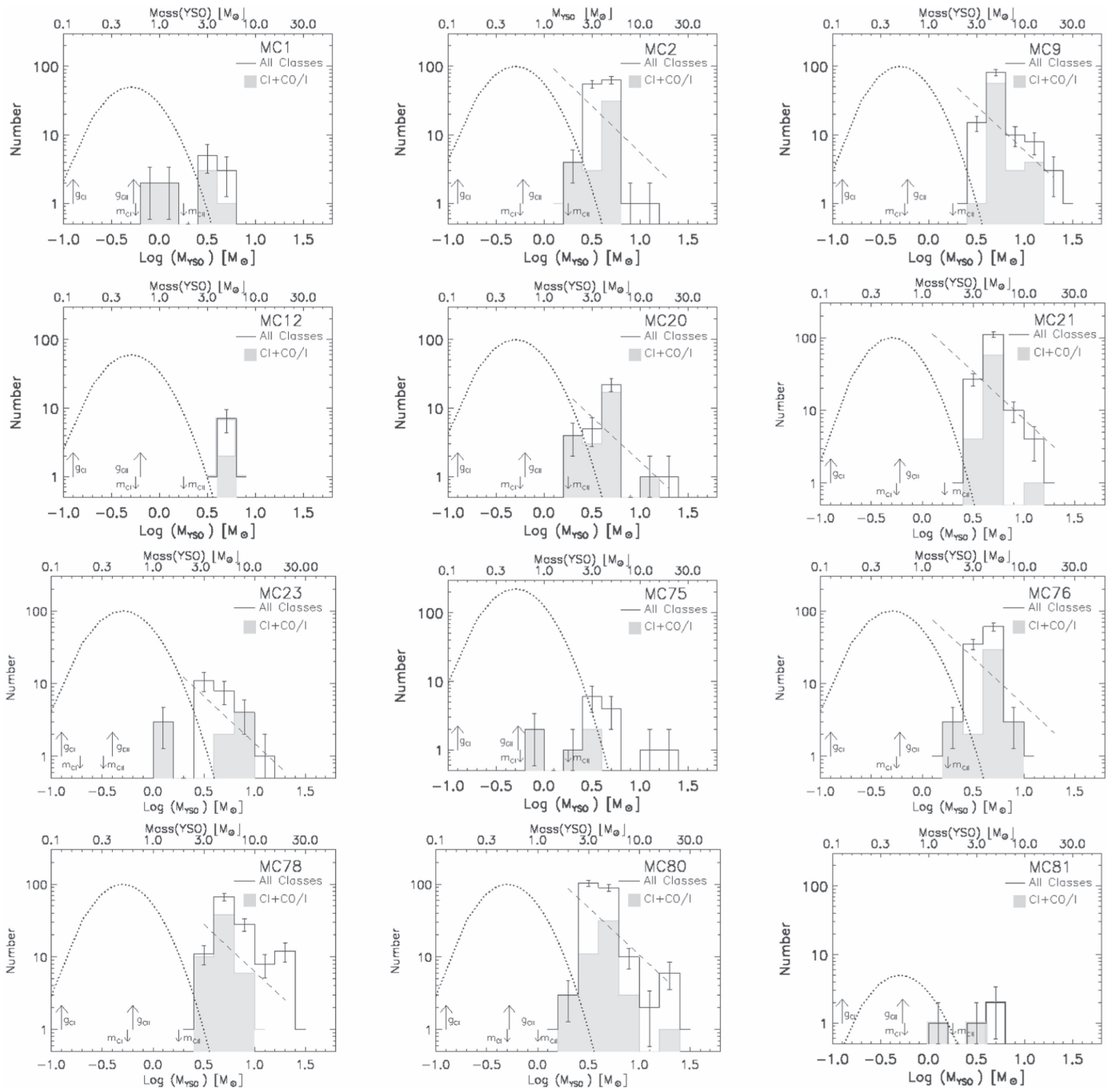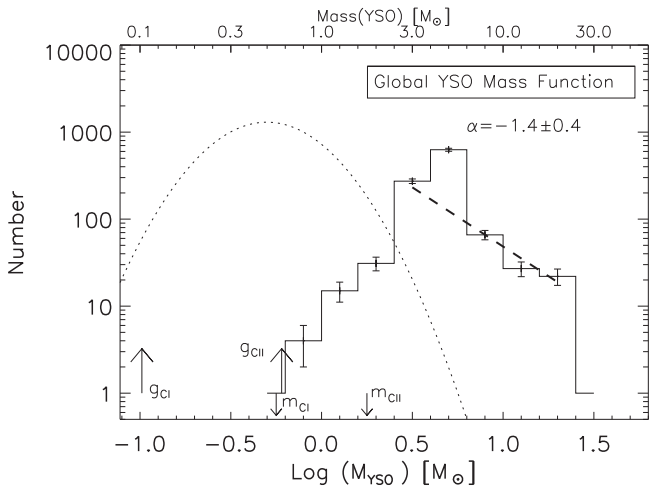
Figure 6. Mass function (MF) of the HLYSOs (shaded histogram) compared to a log-normal Chabrier (2003) IMF (dotted curve) that is normalized for each MC so as to contain the same number of sources as the observed number of LLYSOs in that MC. The contribution of Class I and Class 0/I sources to the histograms is shown by the shaded part. The error bar for each bin of the histogram corresponds to $\sqrt{N}$ statistical uncertainties. The arrows marked with m_{CI}, m_{CII}, g_{CI}, and g_{CII} correspond to the detection limit for Class I and Class II YSOs in MIPSGAL and GLIMPSE surveys, respectively. These values were obtained with the procedure described in Section 3.0. There is clearly an excess number of HLYSOs over the Chabrier (2003) IMF. This excess is well represented by a Salpeter-like IMF (dashed line).

4.4. Age Spread in the Population of YSOs

The more massive a star is, the less time it spends as a YSO. For example, stars more massive than $6 \, M_\odot$ reach the zero-age main sequence in <0.2 Myr (Tognelli et al. 2011). Thus, in a scenario where all stars formed over a period of time shorter than 0.2 Myr (instantaneous), more massive stars are expected to be in later stages of evolution. Given that our HLYSOs are systematically more massive than LLYSOs, we would expect a higher fraction of Class II and Class III sources among HLYSOs as compared to the LLYSOs.

The numbers of YSOs in each Class for HLYSOs and LLYSOs are given in Table 5. The most dominant population among both samples is the Class II, constituting more than 50% and 70% for the HLYSO and LLYSO samples, respectively. This is expected as stars spend most of their PMS lifetime as Class II sources. The fraction of Class III sources is marginally higher for the HLYSO sample as compared to that of the LLYSO sample, as expected in the instantaneous SF scenario. However, in such a scenario, we will not expect Class 0/I sources in the HLYSO sample. The presence of massive stars in these early stages

Figure 7. Mass function (MF) of the HLYSOs (histogram) and the log-normal IMF (dotted curve) of LLYSOs in the 12 clouds. The arrows marked with m_{CI}, m_{CII}, g_{CI}, and g_{CII} correspond to the detection limit for Class I and Class II YSOs in MIPSGAL and GLIMPSE surveys, respectively. The error bar for each bin of the histogram corresponds to $\sqrt{N}$ statistical uncertainties. The high-mass tail of the histogram was fitted with a single power law (dashed line) and resembles the Salpeter-like IMF slope.

suggests that the massive star-formation process is not instantaneous in the majority of our clouds. There are stars of $3\,M_\odot$ in Class III stage in the majority of these clouds, implying star formation, including the formation of massive stars, has started at least 2 Myr ago. Thus, YSOs in our clouds have an age spread of >2 Myr.

The MIPSGAL sources without GLIMPSE counterparts, namely Class I/0 YSOs are an interesting population, especially if these are massive sources. The nature of these massive ($M_{YSO} > 3\,M_\odot$) and bright sources could be linked to the earliest (and brightest) objects in the embedded population. These kinds of sources are associated with (massive) Class 0 YSOs (André et al. 2010) or transitional Class 0/I YSOs. Due to their early evolutionary phase, these objects do not have (detectable) emission at NIR/MIR (André et al. 2010) and must be (only) detected/observed at submillimeter/millimeter spectral range with a weak contribution at 24 μm. The Class I/0 sources could also be confused easily as Class I/II YSOs deeply embedded in the high column density regions of the molecular cloud. Due to the high fraction of the Class I/0 sources, these could be a sum of true Class I/0, and a deeply embedded Class I and Class II YSOs. Indeed, edge-on Class II YSOs with high extinction may be misclassified as Class I objects (Robitaille et al. 2006; Offner & McKee 2011). Nonetheless, the Class I/0 objects without GLIMPSE counterparts are excellent candidates to the embedded prestellar and protostellar core population and constitute the youngest population (from 0.1 Myr to 0.5 Myr age; Enoch et al. 2006; André et al. 2010) of our sample of high-mass star-formation regions. Their MF in a complete sample must give us a clue to the connection between the prestellar and protostellar MF.

4.5. Location of High-mass YSOs in the Clouds

The HLYSOs, for definition, are brighter than $10\,L_\odot$ (Section 4.2). This cut-off luminosity corresponds to a mass of $2\,M_\odot$ for a Class I YSO, whereas it is $\sim3\,M_\odot$ for the Classes II and III YSOs. This implies that all the HLYSOs are of intermediate to high mass. For the purpose of the discussion in
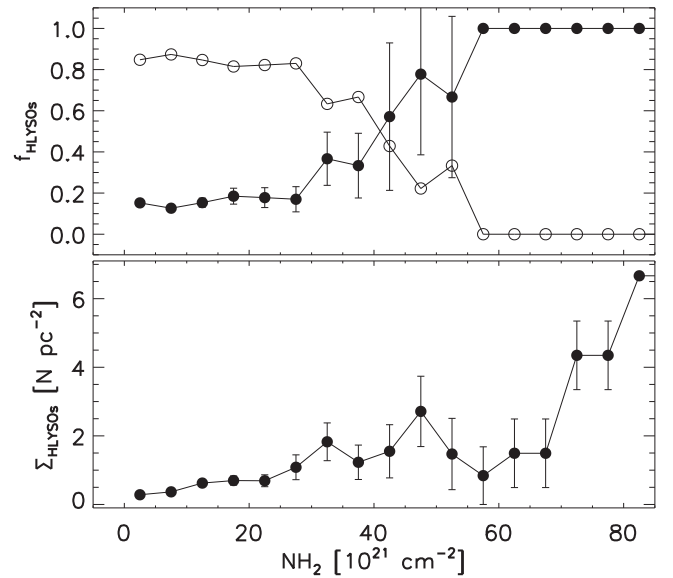

Figure 8. Fraction (top pannel; filled circles) and surface density (bottom pannel; filled circles) of the high-mass YSOs as a function of H_2 column density for our entire MC sample. The fraction of low-mass YSOs is shown with the open circles in the top pannel. The bin width of the plot is $5.0 \times 10^{21}\,cm^{-2}$.

this section, we will refer these YSOs as high-mass YSOs. Recent works (Krumholz & McKee 2008; Lopez-Sepulcre et al. 2010) suggest that a high-density environment is required to form high-mass stars. Thus, the relative fraction of HLYSOs is expected to increase with the surface density of the gas. In order to explore this idea, we plot the ratio $f_{HLYSO} \equiv N(HLYSO)/(N(HLYSO)+N(LLYSO))$ against N_{H_2} in Figure 8. This ratio contains all HMYSO population of the MC sample. The high-mass YSO fraction almost remains constant at ~0.15 up to $\sim3.0 \times 10^{22}\,cm^{-2}$, above which the f_{HLYSO} starts to rise reaching the value of unity at $\sim5.5 \times 10^{22}\,cm^{-2}$. In this gas density range, the surface density of HLYSOs increases from $\sim1\,pc^{-2}$ to more than $6\,pc^{-2}$. In this plot, the fraction of LLYSOs ($1 - f_{HLYSO}$) is shown with open circles. The error bars are obtained assuming a poisson error for each bin in the distribution for both the HLYSOs and total YSOs sample. These errors in the counts are propagated in the ratio defined previously (f_{HLYSO}). The observed tendency agrees very well with the notion that high-mass stars require higher column densities for their formation.

Krumholz & McKee (2008) theoretically addressed the issue of initial physical conditions for the formation of massive stars. They found a minimum density of $1.0\,g\,cm^{-2}$ to be necessary for the formation of the massive stars. However, Galactic star-forming regions are found to harbor high-mass stars at gas densities from 0.1 to $1.0\,g\,cm^{-2}$ (Rathborne et al. 2009; Ragan et al. 2013). In our MCs, the high-mass fraction is 1 above $\sim5.5 \times 10^{22}\,cm^{-2}$, which corresponds to $\sim0.25\,g\,cm^{-2}$. Thus our observed values are consistent with the values observed for other high-mass Galactic clouds.

4.6. Star-formation Rate and Star-formation Efficiency

The values for the SFR in our sample of MCs lie between 16 and $1220\,M_\odot\,Myr^{-1}$, with a median value of $585\,M_\odot\,Myr^{-1}$. These values are comparable to the values of 715 and $159\,M_\odot\,Myr^{-1}$ for Orion A and B, respectively (Lada et al. 2010). SFR varies over a wide range of values in the
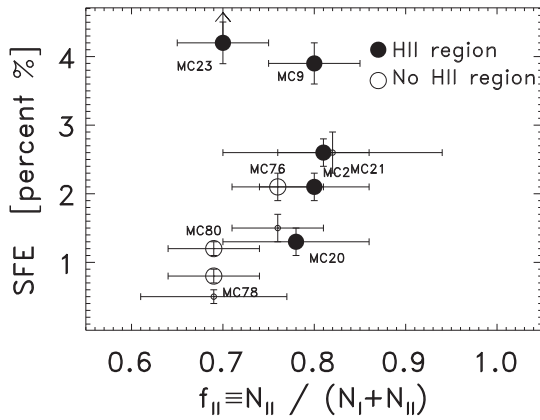
Figure 9. Star-formation efficiency as a function of the Class II fraction in each of our MCs. Clouds containing IRAS sources with UCHII region detected are shown by filled symbols.

Galactic star-forming regions. Vutisalchavakul & Evans (2013) obtained SFR values from ~1 to 2530 $M_{\odot}\,\mathrm{Myr}^{-1}$ for Galactic high-mass star-forming regions at distances of $D > 700$ pc. The values of SFE are in the interval from 0.5% to 3.9%, with MC23 being an outlier with a value of 11.9%. These values are in agreement with values of Orion B (0.6%) and Orion A (2%) star-forming regions (Megeath et al. 2012). However, these values are systematically smaller than the values of ~3% to 6% obtained for nearby low-mass star-forming regions using c2d and GB data (Evans et al. 2009). Values of SFE $\lesssim$ 1% are commonly found for distributed star-forming regions (Bonnell et al. 2011). Half of our clouds have SFE-values $\lesssim$1%, suggesting a distributed SF scenario. Recent studies of young stellar clusters have revealed that there is a time spread in the age of the young stars in stellar clusters (Myers 2012; Foster et al. 2014). Instantaneous mode of cluster formation may apply to compact massive clusters such as Westerlund 1 with high SFE values (Kudryavtseva et al. 2012), but it is possible that low-mass stellar clusters and associations are built up over a long period of time. Thus, SFE is expected to increase with time as more and more stars form. We test this hypothesis below.

In Figure 9, the radio continuum emission detection is denoted by the filled symbol, while no detection is denoted by the open symbol. The f_{II} and the timescale (t_{II}) obtained based on 2.0 ± 1.0 Myr (Evans et al. 2009), are shown in the columns 2 and 3 of the Table 6. The detection or not of radio continuum emission is also included in the same table (column 5).

From the statistics of the YSO population and the molecular cloud mass for the sample of the present study, we can determine some parameters of the star-formation activity such as star-formation rate (SFR) and star-formation efficiency (SFE). The SFR is obtained from the simple expression (Evans et al. 2009), SFR $= M_{YSO}/t_{YSO}$, where the M_{YSO} and t_{YSO} are the "stellar" (YSOs) total mass and the timescale of the YSOs, respectively. The "stellar" masses are obtained by adding the mass of the HLYSO and LLYSO populations. The masses of the HLYSOs are individually obtained following the method already described. The total mass of LLYSOs is derived assuming a mean mass of $0.5\,M_{\odot}$ for every LLYSO. This assumption is equivalent to assuming that the sources follow a log-normal mass distribution with a characteristic mass of $0.5\,M_{\odot}$. We then used the expression $M_{LLYSO}/M_{\odot} = 0.5 \times N_{LLYSO}$ (Evans

et al. 2009), where N_{LLYSO} is the number of LLYSOs. A typical timescales of 2 Myr and 0.54 Myr for the Class II and Class I, respectively, are used for t_{YSO} (Evans et al. 2009). The star-formation efficiency (SFE) is obtained from the expression SFE $\equiv M_{YSO}/(M_{YSO} + M_{cloud})$, where M_{cloud} is the X-factor mass of the molecular cloud (column 6 of Table 2). The resultant SFR and SFE parameters are divided by the cloud area (column 10 of Table 1) to obtain average values of SFR ($\overline{\Sigma}_{SFR}$) and gas density ($\overline{\Sigma}_{gas}$) for our clouds. All these quantities are tabulated in Table 6.

5. Analysis of the Star-formation Law

5.1. Star-formation Law within the Clouds

In order to study the star-formation law within the molecular clouds, we need to obtain the surface density of star-formation rate, Σ_{SFR}, in successive bins of gas surface density, Σ_{gas}. We used the N_{H_2} column density maps derived from the ^{13}CO data in Section 2.1 in order to obtain Σ_{gas}. The lowest Σ_{gas} value corresponds to the MC boundaries that are defined at column densities of $N_{H_2} = 1.0 \times 10^{21}\,\mathrm{cm}^{-2}$ ($A_v = 1$ mag; $\Sigma_{gas} = 20\,M_{\odot}\,\mathrm{pc}^{-2}$). A linear bin in column density is used to define successive values of Σ_{gas}, starting at 1.0×10^{21}, and then taking the values 5.0×10^{21}, 1.0×10^{22}, 1.5×10^{22}, etc. The number of pixels in the ^{13}CO map between successive column density bins are counted to determine the area occupied by the gas at that surface density. The numbers of low- and high-luminosity YSOs between the column density contours are counted, which are then used to calculate the SFR following the methodology described in section Section 4.6. The SFRs are divided by the area occupied by the contours to obtain Σ_{SFR} corresponding to each Σ_{gas}.

The Schmidt law within each cloud in the range of column densities from $N_{H_2} = 1.0 \times 10^{21}\,\mathrm{cm}^{-2}$ to $1.0 \times 10^{23}\,\mathrm{cm}^{-2}$, equivalent to Σ_{gas} range from $20\,M_{\odot}\,\mathrm{pc}^{-2}$ to $2000\,M_{\odot}\,\mathrm{pc}^{-2}$, is shown in Figure 10. For each cloud, data for each gas density bin are plotted with solid circles. The Kennicutt–Schmidt law with $N = 1.4$ is shown by the solid line, whereas the dotted line shows the linear relation of Wu et al. (2005) for massive clumps. In six of the twelve MCs, our points lie between the two lines, whereas in the remaining six, most of our data points lie even above the linear relation of Wu et al. (2005). From a close inspection of the plot for 8 clouds (MC2, MC9, MC12, MC20, MC21, MC23, MC75, and MC76), it can be seen that our data points are not consistent with a power-law fit with a single index (α) (linear in the log-log plane) over the entire range of gas densities. Instead, a broken power-law (BPL) relation seems to be a better fit to the data. Such a relation was found previously by Heiderman et al. (2010) in their data, using separate power laws of the form $y = \alpha x + A$ ($y = \log_{10}(\Sigma_{SFR})$; $x = \log_{10}(\Sigma_{gas})$), one in the low-density regime (index α_1 and coefficient A_1) and the other one in the high-density regime (index α_2 and coefficient A_2). We followed a similar procedure to fit our data points. We fitted two separate lines for the low-density and high-density regimes and obtained the slopes (α_1 and α_2) by following a weighted least-square fitting method, with the weights defined as the inverse square of the errors. The best-fitted lines are shown in the figure, where we also give the slopes α_1 and α_2 for each line. The regression coefficient for each line (R_1 and R_2), as well as the range of data points used for fitting the low- and high-density regimes (x_1 and x_2) are given in Table 7.

Table 6
Star-formation Related Parameters in Our MC Sample

GMC (1)	f_{II} (2)	t_{II} (3)	f_{HL} (4)	Radio (5)	Maser (6)	SFR (7)	$\overline{\Sigma}_{SFR}$ (8)	SFE (9)	$\overline{\Sigma}_{gas}$ (10)
MC2	0.80 ± 0.06	1.98 ± 0.13	0.21 ± 0.03	Yes (1)	CH$_3$O (2)	585 ± 294	2.1 ± 1.1	2.2 ± 0.1	155 ± 79
MC9	0.80 ± 0.05	1.89 ± 0.13	0.14 ± 0.01	Yes (3)	H$_2$O (4)	1105 ± 556	19.1 ± 9.6	3.9 ± 0.2	646 ± 332
MC20	0.78 ± 0.07	2.02 ± 0.14	0.10 ± 0.02	Yes (5)	CH$_3$O (6)	357 ± 182	6.4 ± 3.3	1.2 ± 0.1	647 ± 320
MC21	0.81 ± 0.05	1.99 ± 0.14	0.22 ± 0.02	Yes (7)	...	916 ± 461	2.3 ± 1.2	2.6 ± 0.2	133 ± 60
MC23	0.70 ± 0.05	1.93 ± 0.14	0.05 ± 0.01	Yes (8)	H$_2$O (4)	370 ± 186	26.8 ± 13.5	11.9 ± 0.7	320 ± 240
MC76	0.76 ± 0.05	1.99 ± 0.14	0.15 ± 0.02	No (8)	CH$_3$O (9)	608 ± 306	7.5 ± 3.7	2.1 ± 0.1	565 ± 310
MC78	0.69 ± 0.05	1.97 ± 0.14	0.17 ± 0.02	No (7)	...	1210 ± 610	4.6 ± 2.3	0.8 ± 0.1	763 ± 365
MC80	0.69 ± 0.05	1.83 ± 0.13	0.32 ± 0.03	No (11)	H$_2$O (4)	955 ± 480	5.6 ± 2.8	1.2 ± 0.1	816 ± 410
MC1	0.82 ± 0.12	1.97 ± 0.14	0.08 ± 0.02	Yes (1)	No (4)	77 ± 39	3.3 ± 1.7	2.7 ± 0.3	210 ± 114
MC12	0.69 ± 0.08	2.21 ± 0.16	0.04 ± 0.02	Yes (12)	No (4)	101 ± 52	1.1 ± 0.6	0.5 ± 0.1	358 ± 179
MC75	0.76 ± 0.05	1.99 ± 0.14	0.02 ± 0.01	Yes (13)	No (4)	312 ± 157	5.6 ± 2.8	1.5 ± 0.1	613 ± 320
MC81	0.43 ± 0.30	2.02 ± 0.14	0.28 ± 0.16	Yes (14)	No (4)	16 ± 10	1.0 ± 0.7	0.8 ± 0.3	218 ± 64

Note. Brief explanation of columns: (1) GMC name; (2) fraction of Class II sources defined as $f_{II} = N_{II}/(N_I + N_{II})$; (3) timescale of Class II sources defined as $t_{II} = 2.0 \times (N_I/N_{II}) \times [f_{II}/(1 - f_{II})]$, in [Myr] units; (4) fraction of high-luminosity YSOs defined as $f_{HL} = N(\text{HLYSOs})/N(\text{LLYSOs})$; (5) whether or not radio continuum at centimeter wavelengths (3.6 cm, 4.0 cm, 6 cm, and 21 cm) detected in the cloud. The number in the parenthesis gives the reference of the radio observations, as identified below under References; (6) name of the maser emission if detected. The last four MCs have been targets for the H$_2$O maser, but not detected; the number in the parenthesis gives the reference of the maser observations, as identified below under references; (7) SFR = M_{YSOs}/t_{YSOs} defined in Section 4, in [$M_\odot$ Myr^{-1}] units; (8) Surface density of star formation defined as $\overline{\Sigma}_{SFR}$ = SFR/Area, in [$M_\odot$ Myr^{-1} pc^{-2}] units. Area is given in column 10 of Table 1; (9) star-formation efficiency (in % units) defined as SFE ≡ $100 \times M_{YSOs}/(M_{YSOs}+M_{cloud})$, where M_{cloud} is the M_{XF} given in column 6 of Table 2; and (10) average gas density of the MC defined as $\overline{\Sigma}_{gas} = M_{XF}/\text{Area}$.

References. Meaning of numbers under columns 5 and 6: (1) Urquhart et al. (2009), (2) Lim et al. (2012), (3) Rivera-Ingraham et al. (2010), (4) Codella et al. (1995), (5) Wood & Churchwell (1989), (6) Walsh et al. (1997), (7) Sridharan et al. (2002), (8) Walsh et al. (1998), (9) Walsh et al. (1997), (10) Fontani et al. (2010), (11) Wang et al. (2009), (12) Condon et al. (1998), (13) Kurtz et al. (1994), and (14) Becker et al. (1994).

A minimum of three points is used for the fit in both ranges of densities with the bin(s) at the transition used in either fits. Four MCs (MC1, MC23, M80, and MC81) have too few points and in addition do not offer the dynamical range in Σ_{gas} necessary to carry out a reliable fit (all points lie at Σ_{gas} below $\sim 200\,M_\odot$ pc^{-2}). We hence did not carry out power-law fitting to these clouds. For MC78, only one point lies in the low-density regime, and hence we show only the fit in the high-density regime. The relation is systematically flatter at the low-density regime as compared to that at the high-density regime, with values for the former in the range of 0.2 to 1.0, and the latter 1.3 to 3.0. Note that the SFR is weakly dependent on gas density at low densities with a power-law index <1 in most cases (with the exception of MC21). On the other hand, the power-law index at the high-density regime varies from a similar value (1.3) to the canonical KS index of 1.4 to values as high as 3.6.

The intersection of the two lines in Figure 10 corresponds to the gas surface density value where the break occurs in the star-formation relation. This value is marked by the dashed line in the figure for each cloud and their values are given in Table 7 under the column header Σ_{th}. The break happens at $\Sigma_{gas} = 150-360\,M_\odot$ pc^{-2} in our sample of clouds. The density at the break Σ_{gas} value is often referred to as threshold gas density, Σ_{th}, in the literature. Heiderman et al. (2010), doing a BPL fit similar to that described here, found a threshold value of $129\,M_\odot$ pc^{-2} in nearby low-mass star-forming regions, while Lada et al. (2010) proposed a value of $116\,M_\odot$ pc^{-2} (equivalent to $A_V \sim 8$ mag). Willis et al. (2015) used a $\Sigma_{th} = 200\,M_\odot$ pc^{-2} to obtain the Schmidt law in galactic massive star-forming regions. Our lower threshold values are similar to those reported for other galactic star-forming clouds, while the higher values can be explained if it is considered that the longer distances increase the value of

the threshold density as was reported by Heiderman et al. (2010).

In order to explore if the resulting trend for a BPL fit to the data is statistically significant, we used a total YSO sample for the clouds that show the trend and several fits were tested. This was made for two cases, for all Classes and Class I YSOs. First, in each cloud, the y-value (Σ_{SFR}) was obtained (column 9, Table 7) related to the threshold value in Σ_{gas} (column 8, Table 7). Then each data point of the $\Sigma_{SFR}-\Sigma_{gas}$ plot is divided by this y-value and the resulting data distribution is added in a total normalized sample. In this sample, the best error weighted fit is given by a broken power-law relation with a slight slope for lower densities ($\alpha = 0.6, 0.6$) and steeper slope for higher densities ($\alpha = 2.7, 3.4$), similarly as was previously found in the individual fits for clouds. Therefore, we suggested that the BPL fit is adequate to describe the data point distribution for each cloud with the BPL trend. The fitted parameters are shown in the Table 7 and BPL fit of the normalized samples (all Classes and Class I) is plotted in the Figure 11.

5.2. Global Star-formation Law

We now investigate the position of each cloud as a whole in the global SF law. To do this, we compare the globally averaged values of $\overline{\Sigma}_{SFR}$ and $\overline{\Sigma}_{gas}$ for our clouds (given in Table 6), with the global values for Galactic clouds and clumps obtained in other studies in Figure 12. Our $\overline{\Sigma}_{SFR}-\overline{\Sigma}_{gas}$ values are shown by solid circles, while the data from the study of Heiderman et al. (2010) are plotted with open squares, and the massive dense clumps from Wu et al. (2010) and Heyer et al. (2016) are plotted with diamonds and cross symbols, respectively. The linear relation from Wu et al. (2005) and the Kennicutt relation (Kennicutt 1998) are shown by dashed and solid lines, respectively. Heiderman et al. (2010) found that their global results for low-mass star-forming regions lie above
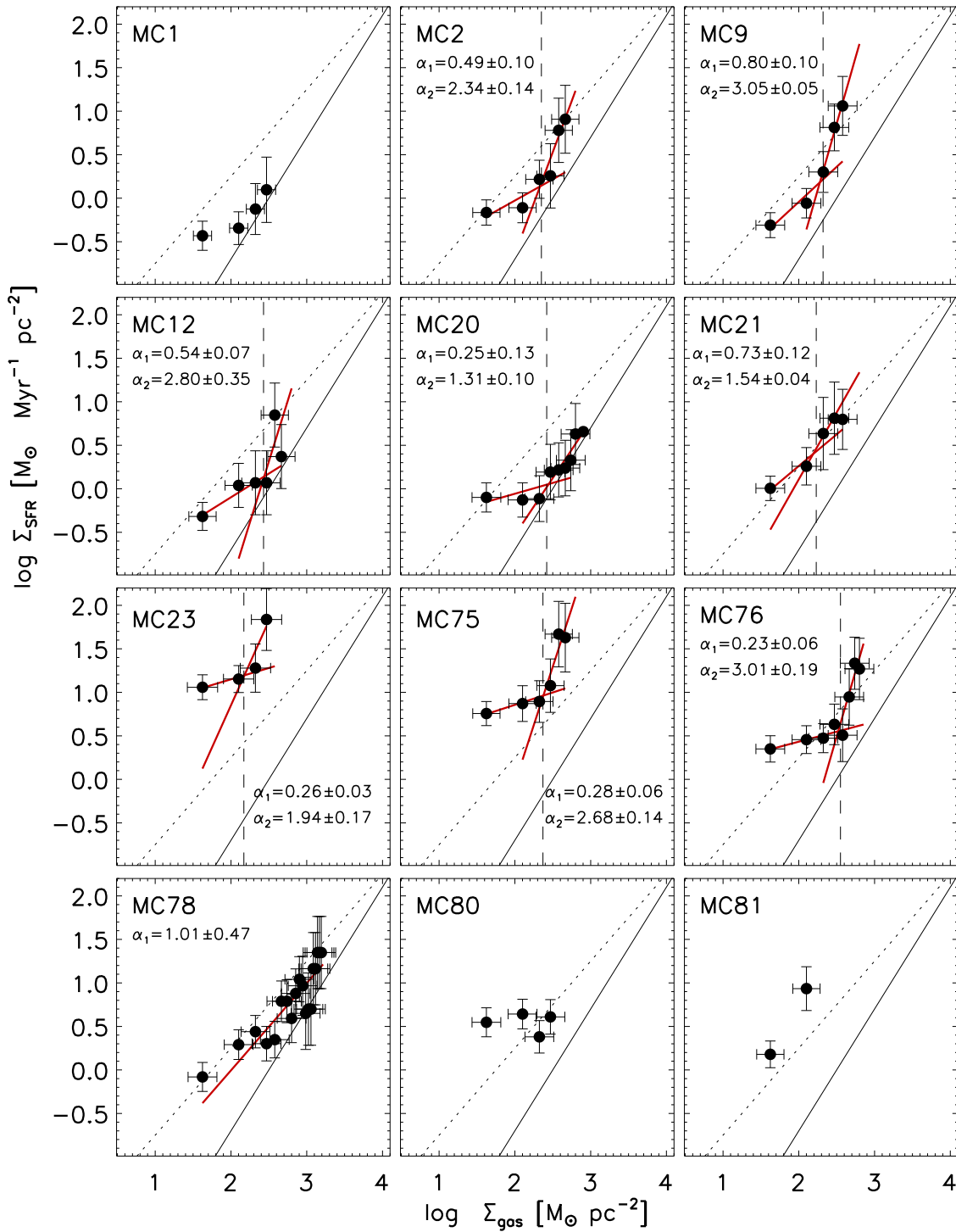
Figure 10. Broken power-law fits in the Σ_{SFR}–Σ_{gas} plane for each sample MC. The power-law indices for the fit in the low (α_1) and high gas density ranges (α_2) are given in the top-left of the plot. The dashed vertical line indicates the density at the break in Σ_{SFR}. The Kennicutt–Schmidt law with $N = 1.4$ (thin solid line) and the Wu et al. (2005) relation (dashed line) are shown for reference.

the KS relation by a factor of up to 17. They found the factors to be as high as 54 for regions containing the youngest sources (Class I and Class Flat). This latter value overlaps with values for the high-density massive clumps of Wu et al. (2010) and Heyer et al. (2016). Our clouds lie between the linear relation of Wu et al. (2005) and the canonical Kennicutt relation, and mostly related to the lower SFR dense clumps from Heyer et al. (2016) and Wu et al. (2010).

In recent work by Heiderman et al. (2010), it has been found that the use of ^{13}CO in the calculation of mass of a molecular cloud results in an underestimation of the mass compared to if visual extinction is used, which is considered a better tracer of the mass of the cloud. According to their results, the mass of the cloud is underestimated by a factor of four to five. If this correction factor is applied in calculating the mass of our sample of clouds plotted in Figure 12, the result is that the

Table 7
Parameters of the Broken Power-law Model Fit

GMC (1)	α (2)	A (3)	σ_α (4)	σ_A (5)	χ^2 (6)	R (7)	Σ_{th} (8)	$y(\Sigma_{th})$ (9)	x_i (10)
MC2	0.49	−1.01	0.10	0.82	0.69	0.71	226.0	1.6	(1–4)
	2.34	−5.33	0.14	2.32	0.19	0.90	…	…	(3–6)
MC9	0.80	−1.65	0.10	0.50	0.30	0.59	211.0	1.0	(1–3)
	3.05	−6.76	0.05	4.06	0.10	0.92	…	…	(3–5)
MC12	0.54	−1.18	0.07	0.44	0.15	0.92	285.0	1.6	(1–4)
	2.80	−6.68	0.35	3.50	0.90	0.64	…	…	(3–6)
MC20	0.25	−0.56	0.13	0.31	0.91	0.82	255.0	1.0	(1–5)
	1.31	−3.14	0.10	1.05	0.27	0.98	…	…	(3–9)
MC21	0.73	−1.19	0.12	0.59	0.20	0.66	180.0	3.2	(1–3)
	1.54	−2.96	0.04	1.71	0.10	0.94	…	…	(2–5)
MC23	0.26	0.63	0.03	0.43	0.10	0.83	150.0	15.9	(1–3)
	1.94	−3.02	0.17	2.17	0.26	0.61	…	…	(2–4)
MC75	0.28	0.29	0.06	0.33	0.14	0.93	237.0	7.1	(1–4)
	2.68	−5.39	0.14	6.29	0.18	0.91	…	…	(3–6)
MC76	0.23	0.01	0.06	0.63	0.22	0.97	360.0	3.1	(1-5)
	3.01	−7.04	0.19	7.75	0.34	0.95	…	…	(4–8)
MC78	1.01	−2.01	0.47	0.27	2.71	0.98	…	…	(1–18)
Total YSOs	0.61	−1.38	0.15	0.07	5.11	0.26	445.0	1.8	(1–30)
	2.69	−6.09	0.33	0.44	3.65	0.35	…	…	(20–48)
Class I YSOs	0.55	−1.70	0.36	0.47	6.68	0.96	380.0	0.5	(1–20)
	3.35	−8.96	1.18	3.85	8.45	0.98	…	…	(16–37)

Note. Brief explanation of columns: the first row lists the fit parameters for the low-density range, while in the next row are shown the fit parameters for the high-density range; (1) GMC name; (2) slope for the linear fit; (3) Y-intercept value of the linear fit; (4) slope error; (5) Y-intercept error; (6) chi-square value for the fit; (7) regression coefficient; (8) gas surface density intersection value (Σ_{th}) in $M_\odot$ pc^{-2} units; (9) Σ_{SFR}-value corresponding to the Σ_{th} in $M_\odot$ Myr^{-1} pc^{-2} units; (10) range of data points used for each linear fit.
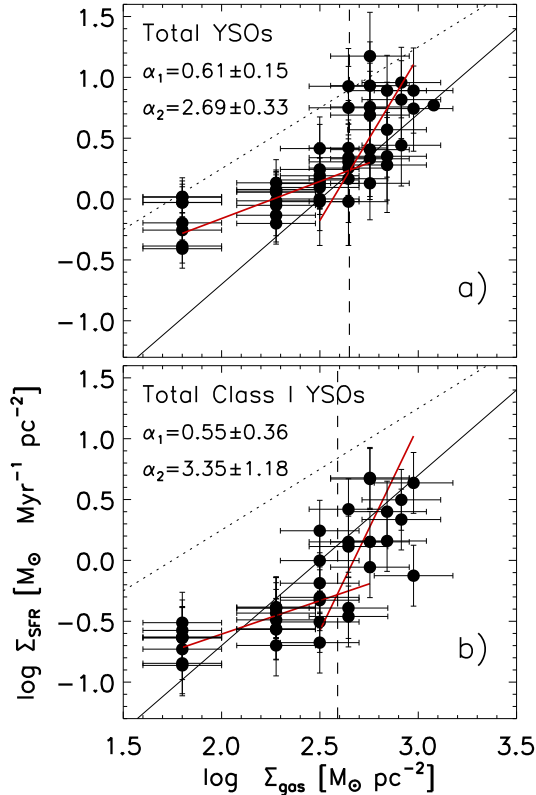
Figure 11. Σ_{SFR}–Σ_{gas} relation for (a) the total of all Classes and (b) Class I YSOs in the clouds that presents the BPL trend. The power-law indices for each gas density range (α_1 and α_2) are given in the top-left of the plot. The dashed vertical line indicates the density at the break in Σ_{SFR}. The Kennicutt–Schmidt law (thin solid line) and the Wu et al. (2005) relation (dotted line) are shown for reference.
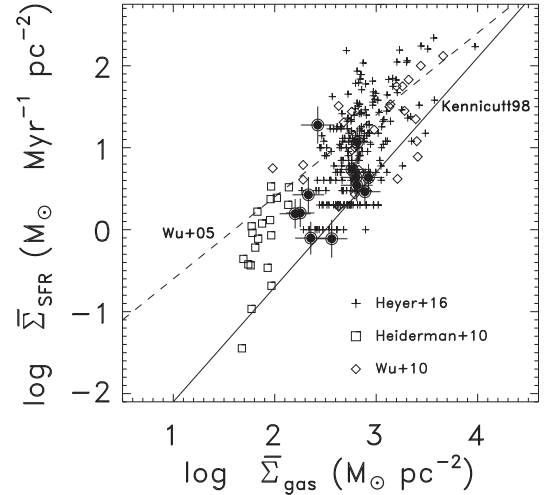
Figure 12. Globally averaged Schmidt law for the clouds. The Kennicutt (1998) relation is plotted with a solid line, while the linear relation of Wu et al. (2005) is plotted with a dashed line. The data of previous studies for galactic star-forming regions are taken from c2d+GB surveys (square symbol; Heiderman et al. 2010) and dense massive clumps (diamond symbol, Wu et al. 2010; cross symbol from Heyer et al. 2016). The filled symbols show the values for the clouds.

values of Σ_{gas} are increased by a value of 0.6 (in log scale) and our distribution follows the distributions for dense clumps reported by Heyer et al. (2016) and Wu et al. (2010) well. The corrected values of our clouds lie on the KS relationship.

It can be noted in the figure that the average gas densities of several MCs from our sample are clustered around log ($\overline{\Sigma}_{gas}$) = 2.6 ± 0.3, compared to clouds from Heiderman et al. (2010) clustered around log(Σ_{gas}) = 2.0. On the other

hand, $\overline{\Sigma}_{gas}$ for the dense clumps are distributed over a much wider dynamic range. Lada et al. (2013) also found an almost constant average $\overline{\Sigma}_{gas}$ for the MCs they analyzed, which they used to argue against the existence of a Schmidt law between MCs. They further argued that the clustering of global $\overline{\Sigma}_{gas}$ is due to the well-known scaling law of Larson (1981) between cloud size and mass, where $\overline{\Sigma}_{gas}$ is a constant for a given value of the limiting column density used to define the MCs. Heyer et al. (2009) found $\overline{\Sigma}_{gas} \sim 40 \, M_{\odot} \, pc^{-2}$ for MCs with a defining boundary of $A_v = 1$ mag. Values obtained in our study are around a factor of four to nine higher, and our lower values compare well with the $\overline{\Sigma}_{gas} \sim 170 \, M_{\odot} \, pc^{-2}$ obtained by Solomon et al. (1987).

5.3. Star Formation below the Threshold Density

The threshold densities, Σ_{th} for our clouds are comparable to the values obtained in the studies of Heiderman et al. (2010) and Lada et al. (2012). However, there is a clear difference in the star-formation relation below Σ_{th} in our clouds as compared to the clouds studied by Heiderman et al. (2010). In the latter study, SF decreases abruptly below Σ_{th}, whereas in our case SF almost remains constant or decreases less steeply with index values being sub-linear below Σ_{th}. This trend below Σ_{th} is also found in the recent study by Willis et al. (2015; see their Figure 9). However, they suspected an increasing contamination from giant stars and background galaxies at decreasing densities as a possible reason for the apparent excess of YSOs below Σ_{th}, and analyzed the star-formation law only for the data points above $\Sigma_{gas} > 200 \, M_{\odot} \, pc^{-2}$.

Is the apparent SF below Σ_{th} an artifact of the method used or is it real? The adopted filtering method (see Section 3) has effectively cleaned our sample of contaminants such as bright foreground/background stars or background galaxies, and hence the presence of YSOs at low densities is real. While calculating the Σ_{SFR}, we have included all YSOs, including those of Class II and III. Heiderman et al. (2010) have used only Class I sources in obtaining the steeply decreasing Σ_{SFR} below Σ_{th}. We now investigate whether the apparent constant Σ_{SFR} below Σ_{th} is due to the inclusion of Class II and III YSOs in our study. In Figure 13, we plot the number (upper panel) and fraction (lower panel) of YSOs separated by Class in each gas density bin. YSOs from all MCs are added at the corresponding gas densities to obtain this plot. It can be seen that Class II sources dominate the observed number of YSOs below Σ_{th}. The Class III fraction remains almost constant at $\sim 10\%$ at all gas densities. Thus, evolved Class III objects do not contribute significantly to Σ_{SFR} below Σ_{th}.

The presence of Class I/II YSOs associated to gas below Σ_{th}, could imply either (1) stellar migration or (2) effect of beam dilution or both. We discuss these two possibilities below.

1. Stellar migration from their birth sites: star-forming cores can migrate from their formation site in a dense environment to the current location. For typical velocities of dense cores of 0.33 to 0.55 km s^{-1} (Muench et al. 2007; Kirk et al. 2010), Class I and II objects can be as far as 1–2 parsecs away from their formation sites. Our clouds measure typically >5 pc, implying the Class I and II YSOs in our clouds had no time to migrate from dense regions to low surface gas density regions.
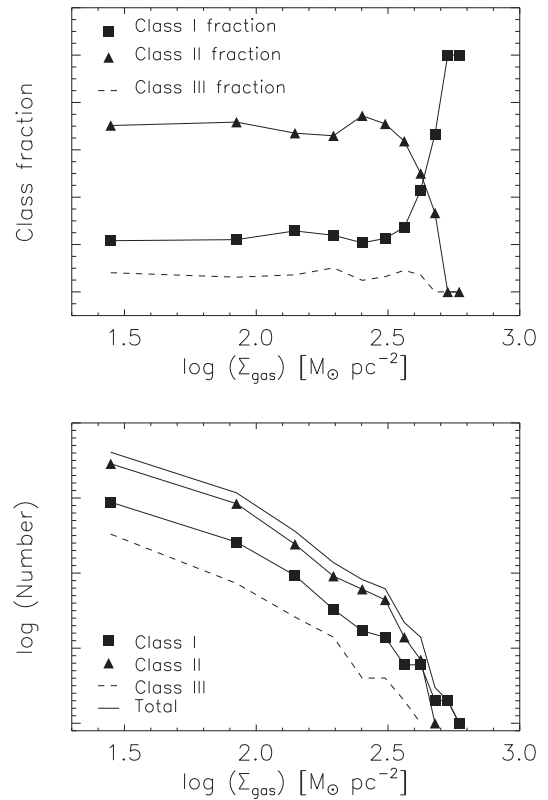
Figure 13. Number (top) and fraction of total (bottom) YSOs separated by Class as a function of surface density of the gas. The range of threshold densities in our sample of clouds is shown by the dotted vertical lines. It can be seen that the relative fractions are almost constant below the threshold density, with the fraction of Class I YSOs increasing steeply at higher densities.

2. Beam dilution: the Σ_{gas} in our study is obtained using ^{13}CO beams (0.3–1.2 pc) that are, in general, larger than the typical core size (0.1 pc). The cores are expected to be surrounded by dense clump gas whose typical size (1 pc) is larger than our beam size. Under such a situation, the observed ^{13}CO column densities are expected to be that of typical clump densities, which would be higher than Σ_{th}. The observed low column densities would then imply that the star-forming cores at densities below Σ_{th} are isolated and are not surrounded by the dense clump gas.

6. Conclusions

Here, we analyzed the local and global star-formation law in a sample of 12 Galactic molecular clouds with signposts of ongoing high-mass star formation. The study is different from similar previous studies in that (1) we investigate the SF relation in the whole cloud, and not just in the dense clumps, and (2) Class-dependent masses are obtained for each MIPS source. The number of high-luminosity sources ($L_{bol} > 10 \, M_{\odot}$) is found to be clearly in excess of that expected for a Chabrier mass function, suggesting a combined Chabrier–Salpeter mass function for the YSOs in our clouds. YSOs with $L_{bol} > 10 \, M_{\odot}$ contribute more than 30% of the total mass in each of our clouds, with a mean value of 55%. The SFR is obtained by the standard technique of counting the YSOs enclosed within contours of gas density as traced by the ^{13}CO emission above $A_v = 1$ mag ($\Sigma_{gas} = 20 \, M_{\odot} \, pc^{-2}$). The relation between Σ_{SFR}

and Σ_{gas} has a break at $\sim$150–360 $M_\odot$ pc^{-2} for almost all of the clouds, with power-law forms on either side of the break, which is also found using the total YSO population of the clouds with the trend. The power-law index above the break lies between 1.3–3.0 in different clouds, which is, in general, higher than the Kennicutt value of 1.4 for extra-galactic regions, but is consistent with the values of Galactic regions found in recent studies. At densities below the break, we find Σ_{SFR} almost independent of density. The density at the break is consistent with the threshold density Σ_{th} found in Galactic and extra-galactic star-forming regions. Globally averaged $\overline{\Sigma}_{gas}$ for our sample of molecular clouds are clustered around a value of 350 $M_\odot$ pc^{-2} within a factor of 2, a range too small to explore a relation with these data alone. The global $\overline{\Sigma}_{SFR}$ lies above the Kennicutt values for the observed $\overline{\Sigma}_{gas}$ by factors between 1 to 60, but agrees within a factor of 2 with the linear relation for massive clumps.

References

Alcalá, J. M., Spezzi, L., Chapman, N., et al. 2008, ApJ, 676, 427
André, Ph., Men'shchikov, A., & Bontemps, S. 2010, A&A, 518, 102
Bastian, N., Covey, K. R., & Meyer, M. R. 2010, ARA&A, 48, 339
Becker, R. H., White, R. L., Helfand, D. J., et al. 1994, ApJS, 91, 347
Benjamin, R. A., Churchwell, E., Babler, B. L., et al. 2003, PASP, 115, 953
Bertin, E., & Arnouts, S. 1996, A&A, 117, 393
Bessell, M. S., & Brett, J. M. 1988, PASP, 100, 1134
Bigiel, F., Leroy, A., Walter, F., et al. 2008, AJ, 136, 2846
Bloemen, J. B. G. M., Strong, A. W., Mayer-Hasselwander, H. A., et al. 1986, A&A, 154, 25
Bolatto, A. D., Wolfire, M., & Leroy, A. K. 2013, ARA&A, 51, 207
Bonnell, I. A., Smith, R. J., Clark, P. C., et al. 2011, MNRAS, 410, 2339
Bronfman, L., Nyman, L.-A., & May, J. 1996, A&A, 115, 81
Burkert, A., & Hartmann, L. 2013, ApJ, 773, 48
Calzetti, D., Liu, G., & Koda, J. 2012, ApJ, 752, 98
Carey, S. J., Noriega-Crespo, A., Mizuno, D. R., et al. 2009, PASP, 121, 76
Chabrier, G. 2003, PASP, 115, 763
Churchwell, E., Babler, B. L., Meade, M. R., et al. 2009, PASP, 121, 213
Churchwell, E., et al. 2005, in GLIMPSE Quality Assurance Document (Madison, WI: Univ. of Wisconsin) (http://astro.wisc.edu/sirtf/GQA-master.pdf)
Clemens, D. P., Sanders, D. B., Scoville, N. Z., & Solomon, P. M. 1986, ApJS, 60, 297
Codella, C., Palumbo, G. G. C., Pareschi, G., et al. 1995, MNRAS, 276, 57
Condon, J. J., Cotton, W. D., Greisen, E. W., et al. 1998, AJ, 115, 1693
Dame, T. M., Hartmann, D., & Thaddeus, P. 2001, ApJ, 547, 792
Deharveng, L., Zavagno, A., Anderson, L. D., et al. 2012, A&A, 546, 74
Dickman, R. L. 1978, ApJS, 37, 407
Dunham, M. M., Allen, L. E., Evans, N. J., II, et al. 2015, ApJS, 220, 11
Ellerbroek, L. E., Bik, A., Kaper, L., et al. 2013, A&A, 558, 102
Enoch, M. L., Evans, N. J., II, Sargent, A. I., & Glenn, J. 2009, ApJ, 692, 973
Enoch, M. L., Young, K. E., Glenn, J., et al. 2006, ApJS, 638, 293
Evans, N. J., II, Allen, L. E., Blake, G. A., et al. 2003, PASP, 115, 965
Evans, N. J., II, Dunham, M. M., Jorgensen, J. K., et al. 2009, ApJS, 181, 321
Faúndez, S., Bronfman, L., Garay, G., et al. 2004, A&A, 426, 97
Fontani, F., Cesaroni, R., & Furuya, R. S. 2010, A&A, 517, A56
Foster, J. B., Arce, H. G., Kassis, M., et al. 2014, arXiv:1407.6003F
Gao, Y., & Solomon, P. M. 2004, ApJ, 606, 271
Goto, M., Usuda, T., Takato, N., et al. 2003, ApJ, 598, 1038

Greene, T. P., Wilking, B. A., Andre, P., et al. 1994, ApJ, 434, 614
Gutermuth, R. A., & Heyer, M. 2015, AJ, 149, 64
Gutermuth, R. A., Megeath, S. T., Myers, P. C., et al. 2009, ApJS, 184, 18
Gutermuth, R. A., Myers, P. C., Megeath, S. T., et al. 2008, AJ, 674, 336
Gutermuth, R. A., Pipher, J. L., Megeath, S. T., et al. 2011, AJ, 739, 84
Hartmann, L., Megeath, S. T., Allen, L., et al. 2005, ApJ, 629, 88
Hartmann, L. W., & Kenyon, S. J. 1996, ARA&A, 34, 207
Harvey, P. M., Chapman, N., Shih-Ping, L., et al. 2006, ApJ, 644, 307
Heiderman, A., & Evans, N. J., II 2015, ApJ, 806, 231
Heiderman, A., Evans, N. J., II, Allen, L. E., et al. 2010, ApJ, 723, 1019
Heyer, M., Gutermuth, R., Urquhart, J. S., et al. 2016, A&A, 588, A29
Heyer, M., Krawczyk, C., Duval, J., & Jackson, J. M. 2009, ApJ, 699, 1092
Hillenbrand, L. A., & White, R. L. 2004, ApJ, 604, 741
Jackson, J. M., Rathborne, J. M., Shah, R. Y., et al. 2006, ApJ, 163, 145
Kennicutt, R. C. 1998, ApJ, 498, 541
Kennicutt, R. C., & Evans, N. J. 2012, ARA&A, 50, 531
Kenyon, S. J., & Hartmann, L. 1995, ApJS, 101, 117
Kenyon, S. J., Hartmann, L. W., Strom, K. M., et al. 1990, AJ, 99, 869
Kirk, H., Pineda, J. E., Johnstone, D., et al. 2010, ApJ, 723, 457
Krumholz, M. R., & McKee, C. F. 2008, Natur, 451, 1082
Kryukova, E., Megeath, S. T., Gutermuth, R. A., et al. 2012, AJ, 144, 31
Kudryavtseva, N., Brandner, W., Gennaro, N., et al. 2012, ApJ, 750, 44
Kurtz, S., Churchwell, E., & Wood, D. O. S. 1994, ApJS, 91, 659
Lada, C. J. 1987, in IAU Symp. 115, Star-forming Regions, ed. M. Peimbert & J. Jugaku (Dordrecht: Reidel), 1
Lada, C. J., Forbrich, J., Lombardi, M., & Alves, J. F. 2012, ApJ, 745, 190
Lada, C. J., Lombardi, M., & Alves, J. F. 2010, ApJ, 724, 687
Lada, C. J., Lombardi, M., Roman-Zuniga, C., Forbrich, J., & Alves, J. F. 2013, ApJ, 778, 133
Lada, C. J., & Wilking, B. A. 1984, ApJ, 287, 610
Larson, R. B. 1981, MNRAS, 194, 809
Lim, W., Lyo, A., Kim, K., et al. 2012, AJ, 144, 151
Lopez-Sepulcre, A., Cesaroni, R., & Walmsley, C. M. 2010, A&A, 517, A66
MacLaren, I., Richardson, K. M., & Wolfendale, A. W. 1988, ApJ, 333, 821
Marengo, M., Reiter, M., & Fazio, G. G. 2008, in AIP Conf. Proc. 1001, IXth Torino Workshop on Evolution and Nucleosynthesis in AGB Stars and the IInd Perugia Workshop on Nuclear Astrophysics, ed. R. Guandalini, S. Palmerini, & M. Busso (Melville, NY: AIP), 331
May, J., Alvarez, H., & Bronfman, L. 1997, A&A, 327, 325
Megeath, S. T., Gutermuth, R., Muzerolle, J., et al. 2012, AJ, 144, 192
Muench, A. A., Lada, C. J., Rathborne, J. M., et al. 2007, ApJ, 671, 1820
Myers, P. C. 2012, ApJ, 752, 9
Myers, P. C. 2014, ApJ, 781, 33
Offner, S. S. R., & McKee, C. F. 2011, ApJ, 736, 530
Palla, M. M., & Stahler, H. G. 1993, ApJ, 418, 414
Pineda, J. E., Caselli, P., & Goodman, A. A. 2008, ApJ, 679, 481
Ragan, S. E., Henning, T., & Beuther, H. 2013, A&A, 559, 79
Rathborne, J. M., Jackson, J. M., Simon, R., et al. 2009, Ap&SS, 324, 155
Rieke, G. H., Young, E. T., Engelbracht, C. W., et al. 2004, ApJS, 154, 25
Rivera-Ingraham, A., Ade, P. A. R., Bock, J. J., et al. 2010, ApJ, 723, 915
Robitaille, T. P., Whitney, B. A., Indebetouw, R., et al. 2006, ApJS, 167, 256
Salpeter, E. E. 1955, ApJ, 121, 161
Sanders, D. B., Clemens, D. P., Scoville, N. Z., & Solomon, P. M. 1986, ApJ, 60, 1
Saral, G., Hora, J. L., Willis, S. E., et al. 2015, ApJ, 813, 25
Schmidt, M. 1959, ApJ, 129, 243
Simon, R., Jackson, J. M., Clemens, D. P., et al. 2001, ApJ, 551, 747
Solomon, P. M., Rivolo, A. R., Barrett, J., & Yahil, A. 1987, ApJ, 319, 730
Sridharan, T. K., Beuther, H., Schilke, P., et al. 2002, ApJ, 566, 931
Stahler, S. W., & Palla, F. 2005, The Formation of Stars (New York: Wiley-VCH)
Tognelli, E., Prada Moroni, P. G., & Degl'Innocenti, S. 2011, A&A, 533, 109
Urquhart, J. S., Hoare, M. G., Purcell, C. R., et al. 2009, A&A, 501, 539
Vorobyov, E. I., & Basu, S. 2005, ApJ, 633, 137
Vutisalchavakul, N., & Evans, N. J., II 2013, ApJ, 765, 129
Walsh, A. J., Burton, M. G., Hyland, A. R., et al. 1998, MNRAS, 301, 640
Walsh, A. J., Hyland, A. R., Robinson, G., et al. 1997, MNRAS, 291, 261
Wang, K., Wu, Y. F., Ran, L., et al. 2009, A&A, 507, 369
Willis, S., Guzman, A., Marengo, M., et al. 2015, ApJ, 809, 87
Wood, D. O. S., & Churchwell, E. 1989, ApJ, 340, 265
Wu, J., Evans, N. J., II, Gao, Y., et al. 2005, ApJL, 635, 173
Wu, J., Evans, N. J., II, Shirley, Y. L., et al. 2010, ApJS, 188, 313